

Calorimetry

Richard Wigmans

Department of Physics, Texas Tech University, Lubbock, TX 79409-1051, U.S.A.
wigmans@ttu.edu

This paper is intended as an introduction to and overview of calorimetric particle detection in high-energy physics experiments. It is a write-up of lectures given in the context of the “Dottorato di Ricerca in Fisica dell’ Università di Pavia” in May 2006. First, the physics that plays a role when high-energy particles are absorbed in dense matter is described, with emphasis on issues that are important for the properties of calorimeters. Next, all aspects of the calorimeter response function are discussed: mean value, shape, width, and the factors that determine these characteristics. Then, we elaborate on some practical issues that are important for those working with calorimeters: calibration and simulation. Finally, a brief overview of modern developments in this rapidly evolving field is given.

TABLE OF CONTENTS

1. Introduction	18
2. The Physics of Shower Development	19
2.1. Electromagnetic showers	19
2.2. Hadronic showers	23
2.3. Lessons for calorimetry	24
3. The Calorimeter Response Function	27
3.1. Absolute response and response ratios	27
3.2. Compensation	31
3.3. Fluctuations	33
3.4. The shape of the response function	37
3.5. Lessons for calorimeter design	39
4. Calibration and Simulation	41
4.1. Calibration	41
4.2. Monte Carlo simulations	47
5. The Future of Calorimetry	48
5.1. The Energy Flow Method	49
5.2. Off-line compensation	49
5.3. Dual-readout calorimetry	51
6. Outlook	55

1 Introduction

Calorimeters were originally developed as crude, cheap instruments for some specialized applications in particle physics experiments, such as detection of neutrino interactions. However, in the past 25 years, their role has changed considerably. In modern colliders, calorimeters form the heart and the soul of the experiments. They fulfill a number of crucial tasks, ranging from event selection and triggering to precision measurements of the fourvectors of individual particles and jets and of the energy flow in the events (missing energy, *etc.*). This development has benefitted in no small part from the improved understanding of the working of these, in many respects somewhat mysterious, instruments.

The contribution of calorimeter information to the data analysis focuses in many experiments primarily on particle identification (electrons, γ s, muons) and on the energy measurement of particles that develop

electromagnetic (em) showers (e, γ, π^0). In ep and $p\bar{p}$ experiments, and especially in experiments at a future linear e^+e^- collider, calorimetric energy measurement of hadrons and jets is also important. The importance of hadron calorimetry is expected to increase considerably as the collision energy is further increased.

Calorimeters are highly non-trivial instruments. Many subtle effects conspire to determine their performance. This paper is intended as a compact introduction to and overview of the subject of calorimetry and its applications in detectors for high-energy particle physics. It is subdivided in chapters which address the following topics:

1. The physics of shower development
2. The calorimeter response function
3. Calibration and simulation
4. R&D to further improve (our understanding of) calorimetry

For more complete and extensive coverage of the material contained in this paper, the reader is referred to Reference [1].

2 The Physics of Shower Development

Although calorimeters are intended to measure energy deposits at the level of 10^9 eV and up, their performance is in practice determined by what happens at the MeV, keV and sometimes eV levels. Since showers initiated by hadrons, such as protons and pions, are distinctly different (and in particular more complicated) than the electromagnetic (em) ones initiated by electrons or photons, we will start with the latter.

2.1 Electromagnetic showers

The processes that play a role in em shower development are few and well understood. Electrons and positrons lose energy by *ionization* and by *radiation*. The first process dominates at low energy, the second one at high energy. The *critical energy*, at which both processes play equally important roles, is roughly inversely proportional to the Z value of the absorbing medium.

$$\epsilon_c = \frac{610 \text{ MeV}}{Z + 1.24} \quad (1)$$

Photons interact either through the *photoelectric effect*, *Compton scattering* or *pair production*. The photoelectric effect dominates at low energies, pair production at high energies (Figure 1). The relative cross sections are also Z dependent. For example, the cross section for photoelectron production is proportional to Z^5 and E^{-3} , while the cross section for pair production gradually increases, both with Z and with E , to reach an asymptotic value near ~ 1 GeV. The *angular distribution* is more or less isotropic for the photo- and Compton electrons, but highly directional for the e^+e^- pairs produced in pair production.

At energies of 1 GeV and higher, electrons and photons initiate *em showers* in the materials in which they penetrate. Electrons lose their energy predominantly by radiation, the most energetic photons produced in this process convert into e^+e^- pairs, which radiate more γ s, *etc.* The number of shower particles produced in this particle multiplication process reaches a maximum (the *shower maximum*) at a certain depth inside the absorber, and gradually decreases beyond that depth (Figure 2a). The depth of the shower maximum increases (logarithmically) with the energy of the incoming electron. Because of the particle multiplication, the total amount of material needed to contain em showers is relatively small. For example, when 100 GeV electrons enter lead, 90% of their energy is deposited in only 4 kg of material.

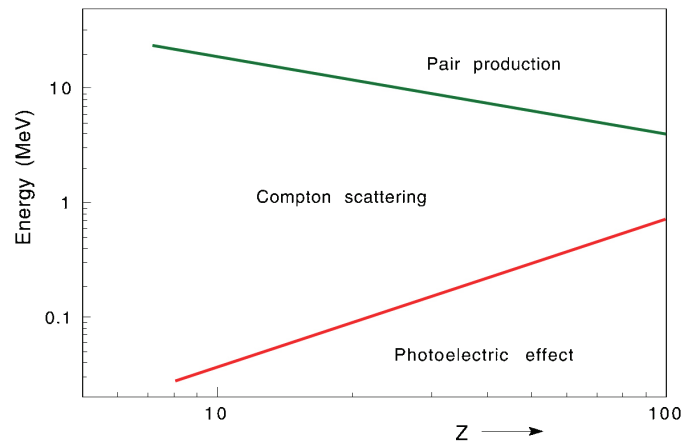


Fig. 1: The energy domains in which photoelectric effect, Compton scattering and pair production are the most likely processes to occur, as a function of the Z of the absorber material.

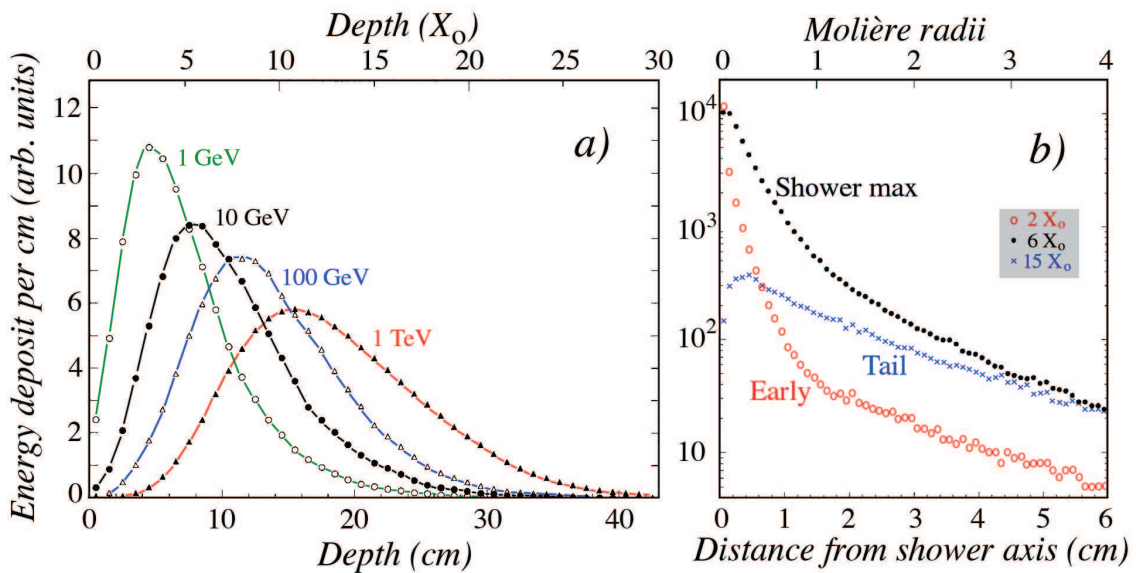


Fig. 2: The energy deposited as a function of depth for 1, 10, 100 and 100 GeV electron showers developing in a block of copper. In order to compare the shower profiles, the integrals of these curves have been normalized to the same value (a). The radial distributions of the energy deposited by 10 GeV electron showers in copper, at various depths (b). Results of EGS4 calculations.

The lateral development of em showers is governed by two types of processes:

1. Electrons and positrons move away from the shower axis because of multiple scattering.
2. Photons and electrons produced in isotropic processes (Compton scattering, photoelectric effect) move away from the shower axis.

The first process dominates in the early stages of the shower development, the second one beyond the shower maximum. Both processes have their own characteristic, exponential scale. The two components

are distinctly visible in Figure 2b, which shows the radial energy density for electron showers developing in copper, at three different depths inside the calorimeter.

The shower development can be described more or less independently of the details of the absorber material in terms of the *radiation length* (for the longitudinal development) and the *Molière radius* (for the lateral development). Both units are defined for the asymptotic energy regime (> 1 GeV). The radiation length (X_0) is the ratio of the electron energy and the specific energy loss by radiation. Therefore, a high-energy electron loses on average 63% ($1 - e^{-1}$) of its energy when it traverses $1X_0$ of material. The mean free path of a high-energy photon equals $9X_0/7$. The Molière radius (ρ_M) is defined through the ratio of the radiation length and the critical energy. When expressed in g/cm^2 , X_0 scales as A/Z^2 and ρ_M as A/Z . Therefore, ρ_M is much less material dependent than X_0 . For example, copper and lead have approximately the same value for ρ_M , while their radiation lengths differ by a factor of 3.

The radiation length has a fundamentally different meaning for electrons and photons. Showers initiated by high-energy electrons and by photons develop initially quite differently. When they encounter material, high-energy electrons start to radiate immediately. On their way through a few mm of material, they may emit thousands of bremsstrahlung photons. On the other hand, high-energy photons may or may not convert in the same amount of material. In the latter case, they do not lose any energy, and when they convert early on, they may lose as much as, or even more than, electrons in the same amount of material. This difference is illustrated in Figure 3. In the same amount of material (in this example $5X_0$), electrons lose on average a larger fraction of their energy than photons, but the spread in the energy losses by photons is larger.

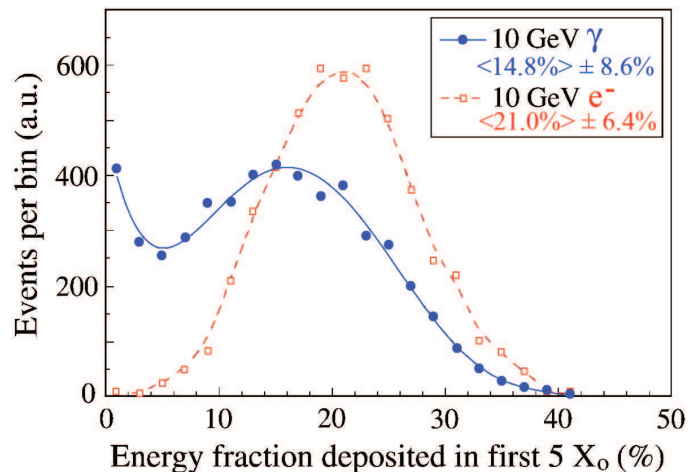


Fig. 3: Distribution of the energy fraction deposited in the first 5 radiation lengths by 10 GeV electrons and γ s showering in lead. Results of EGS4 calculations [2].

Even though the em shower profiles scale, in first approximation, with X_0 and ρ_M , this scaling is not perfect. This is illustrated in Figure 4. The differences may be understood from the fact that the particle multiplication continues down to lower energies in high- Z material and decreases more slowly beyond the shower maximum. For example, a given high-energy electron produces 3 times more positrons when showering in lead than in aluminium. As a result, one needs more X_0 of lead than of aluminium to contain this shower at the 99% level. Also, the shower maximum is located at a greater depth in lead. These features are confirmed by Figure 4.

The material dependence of the calorimeter thickness needed to contain electron showers is shown in Figure 5b. For 99% containment, the difference between high- Z and low- Z absorber materials may be as much as $10X_0$. And for reasons described above, it takes even more material to contain γ induced showers. The energy dependence of the calorimeter thickness needed to contain em showers is shown in Figure 5a.

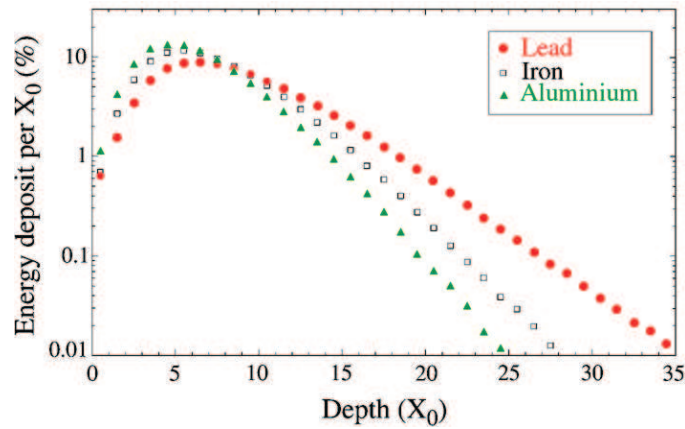


Fig. 4: Longitudinal profiles of 10 GeV e^- showers developing in aluminium ($Z = 13$), iron ($Z = 26$) and lead ($Z = 82$).

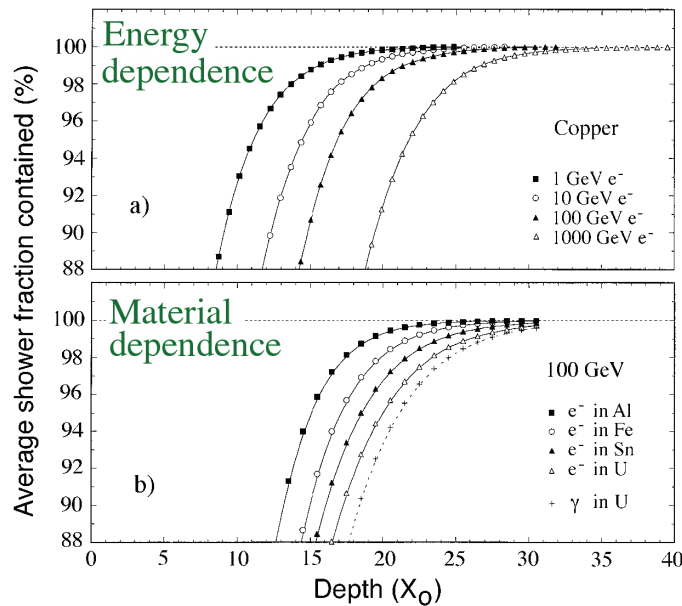


Fig. 5: Average energy fraction contained in a block of matter with infinite transverse dimensions, as a function of the thickness of the absorber. Shown are results for showers induced by electrons of various energies in a copper absorber (a) and results for 100 GeV electron showers in different absorber materials (b). Results of EGS4 calculations.

For lateral shower containment, material differences are much smaller than longitudinally. In addition, there is no energy dependence. A given (sufficiently long) cylinder will thus contain the same fraction of the energy from 1 GeV em showers as from 1 TeV ones.

Deviations from scaling as observed in Figures 4 and 5 are caused by phenomena that occur at energies below the critical energy. For example, in lead more than 40% of the shower energy is deposited by particles with energies below 1 MeV, while the critical energy is ~ 7 MeV. Only one quarter of the energy is deposited by positrons, the rest by electrons. These facts, which are derived from EGS4 Monte Carlo simulations of em shower development, illustrate that Compton scattering and photoelectron production

are very important processes for understanding calorimetry. Both processes dominate at energies far below the critical energy and are therefore not properly described by scaling variables such as X_0 and ρ_M .

2.2 Hadronic showers

In showers developed by hadrons, an additional complication arises from the role played by the *strong interaction*. This interaction is responsible for:

1. The production of hadronic shower particles. The vast majority of these, $\sim 90\%$, are pions. The neutral pions decay in 2γ s, which develop em showers.
2. The occurrence of nuclear reactions. In these processes, neutrons and protons are released from atomic nuclei. The nuclear binding energy of these nucleons *has to be provided*. Therefore, the fraction of the shower energy needed for this purpose does not contribute to the calorimeter signals. This is the so-called *invisible-energy* phenomenon.

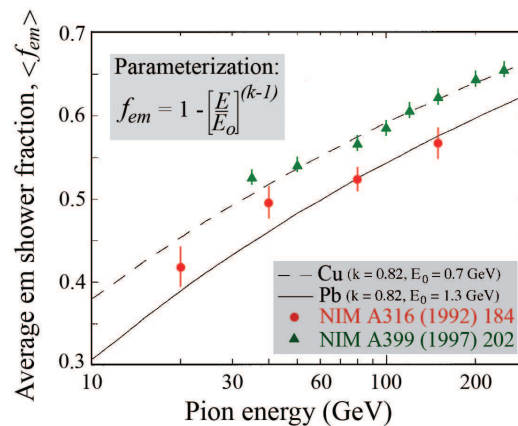


Fig. 6: Comparison between the experimental results on the em fraction of pion-induced showers in copper-based and lead-based calorimeters [3,4].

The em showers initiated by π^0 s develop in the same way as those initiated by high-energy photons. The fraction of the shower energy carried by this em component (called f_{em} in the following) varies strongly from event to event. On average, this fraction increases with the shower energy, since π^0 s may also be (and are, see Figure 7) produced by secondary and higher-order shower particles: the larger the shower energy, the more generations of shower particles, the larger f_{em} . Typically, f_{em} increases from $\sim 30\%$ at 10 GeV to $\sim 50\%$ at 100 GeV (Figure 6). In a typical hadron shower developing in lead, the remaining (non-em) energy is deposited in the following way: ionizing particles (56%, two thirds from protons), neutrons (10%), invisible energy (34%). The neutrons are very soft (typically 3 MeV), on average there are 37 neutrons per GeV deposited energy. The protons (which dominate the non-em signals from calorimeters) originate primarily from nuclear spallation processes, they carry typically 50 - 100 MeV a piece. These numbers illustrate that the large majority of the non-em energy is deposited through *nucleons* and *not* through relativistic particles such as pions.

These characteristics have important consequences for calorimetry:

- As a result of the invisible-energy phenomenon, the calorimeter signals for hadrons are in general smaller than for electrons of the same energy (*non-compensation*).
- Since the em energy fraction is energy dependent, the calorimeter is *non-linear* for hadron detection.

The hadronic shower profiles are governed by the *nuclear interaction length* (λ_{int}), *i.e.*, the average distance hadrons travel before inducing a nuclear interaction. This interaction length, expressed in g/cm^2 , scales with $\sqrt[3]{A}$. On average, hadronic shower profiles look very similar to the em ones displayed in Figure 2, except that the scale factor is usually much larger for the hadronic showers. For example, for copper X_0 amounts to 1.4 cm, while $\lambda_{\text{int}} = 15$ cm.

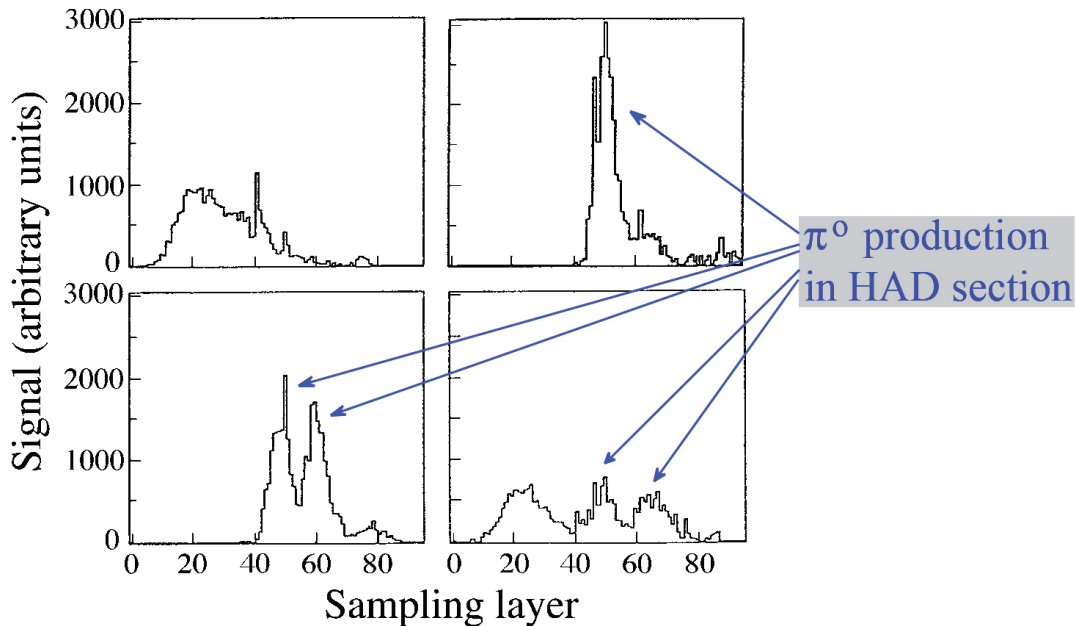


Fig. 7: Longitudinal profiles for 4 different showers induced by 270 GeV pions in a lead/iron/plastic-scintillator calorimeter [5].

Another important difference between em and hadronic showers is the large variety of profiles for the latter. This is illustrated in Figure 7, which shows 4 different showers induced by 270 GeV pions. The strange shapes result from the production of energetic π^0 s in the second or third generation of the shower development.

Just as for em showers, the depth of the calorimeter needed to contain hadronic showers to a certain degree increases logarithmically with energy (Figure 8). However, because of the large longitudinal fluctuations in shower development (Figure 7), leakage effects might still play an important role, even though the calorimeter contains the showers, on average, to 99%. Laterally, it takes *less* material to contain high-energy showers than low-energy ones (Figure 9). This is a consequence of the fact that the em shower fraction increases with energy. The em showers produced by π^0 s tend to develop close to the shower axis.

The difference between λ_{int} and X_0 , which may be as large as a factor 30 in high- Z materials, is fruitfully used to distinguish between em and hadronic showers. A simple piece of lead (0.5 cm thick) followed by a sheet of scintillating plastic makes a very effective *preshower detector*, as illustrated in Figure 10.

2.3 Lessons for calorimetry

Based on the shower characteristics discussed above, we can draw some very important conclusions for the design of calorimeters:

- In the absorption processes that play a role in calorimeters, most of the energy is deposited by *very soft shower particles*. In em showers and shower components, photo- and Compton electrons contribute

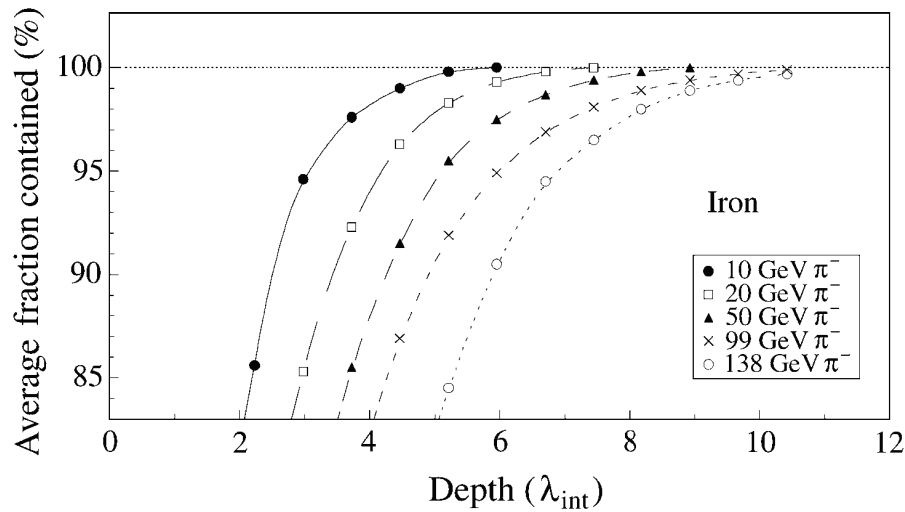


Fig. 8: Average energy fraction contained in a block of matter with infinite transverse dimensions, as a function of the thickness of the absorber [6].

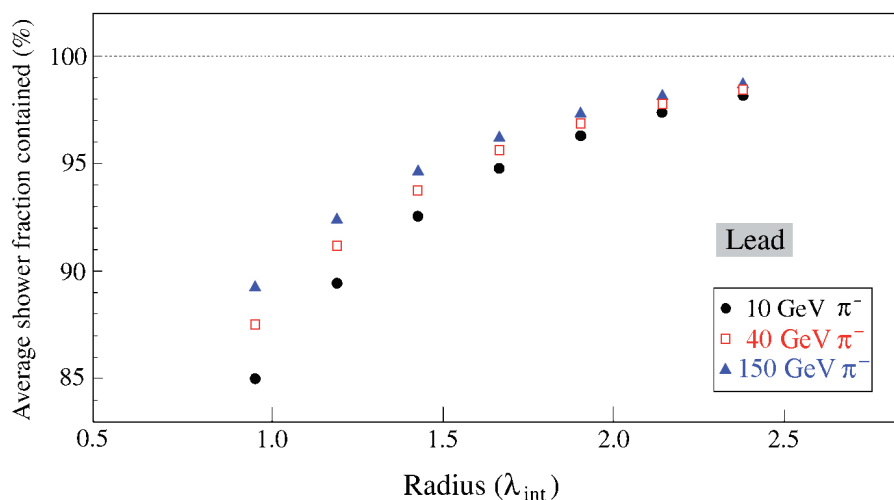


Fig. 9: Average energy fraction contained in an infinitely long cylinder of absorber material, as a function of the radius of this cylinder, for pions of different energies showering in a lead-based calorimeter [3].

in a major way to the energy deposit process and thus to the calorimeter signals. Because of their isotropic angular distribution, these shower particles have “forgotten” the direction of the incoming particle (Figure 11). As a result, it does not matter how one chooses to orient the active layers in a sampling calorimeter. Originally, it was believed that only a “sandwich” calorimeter structure would work. Nowadays, there are a wide variety of geometries in use, including fiber structures with fibers running in the same direction as the showering particles. Such alternative structures may offer considerable advantages, *e.g.*, in terms of hermeticity, signal speed, *etc.*

- The typical shower particle in em showers is a 1 MeV electron. The range of such a particle is very short, less than 1 mm in typical absorber materials such as iron or lead. This range, rather than the radiation length, sets the scale for a useful sampling frequency in em calorimeters.

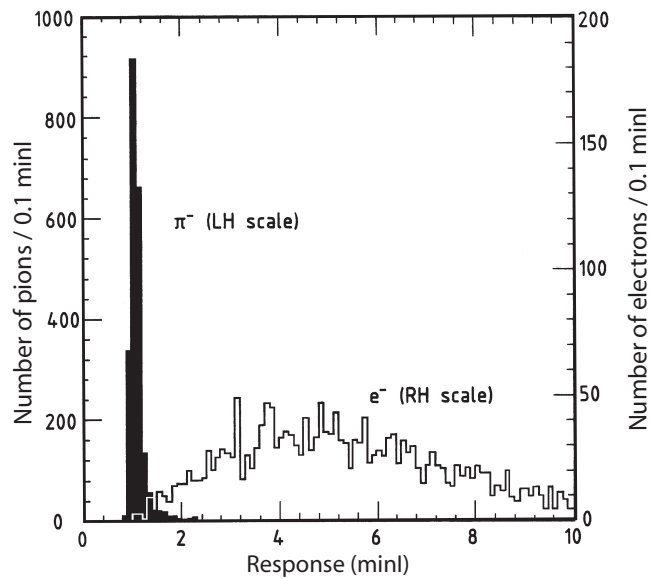


Fig. 10: Signal distributions for 75 GeV π^- and e^- in a very simple preshower detector.

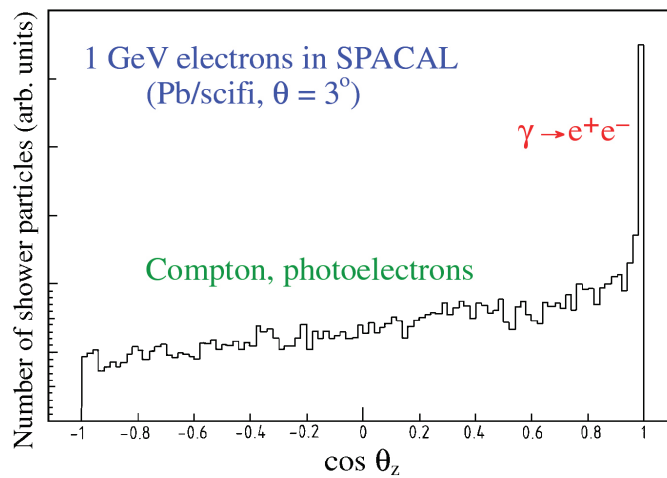


Fig. 11: Angular distribution of the shower particles (e^+ , e^-) through which the energy of a 1 GeV electron is absorbed in a lead-based calorimeter [7].

- Typical shower particles in hadron showers are 50 - 100 MeV spallation protons and 3 MeV neutrons. The range of such protons is typically ~ 1 cm. This sets the scale for a useful sampling frequency in hadron calorimeters. The neutrons travel typically several cm between interactions. Neutrons are only important for the signals from sampling calorimeters if they have a sufficiently large probability of interacting in the active material and generate measurable reaction products. Figure 12 shows an example of a type of event that plays a dominant role in hadronic shower development. In such nuclear reactions, large numbers of nucleons are released, and the energy with which they were bound in the struck nucleus (~ 8 MeV/nucleon) is lost for detection.

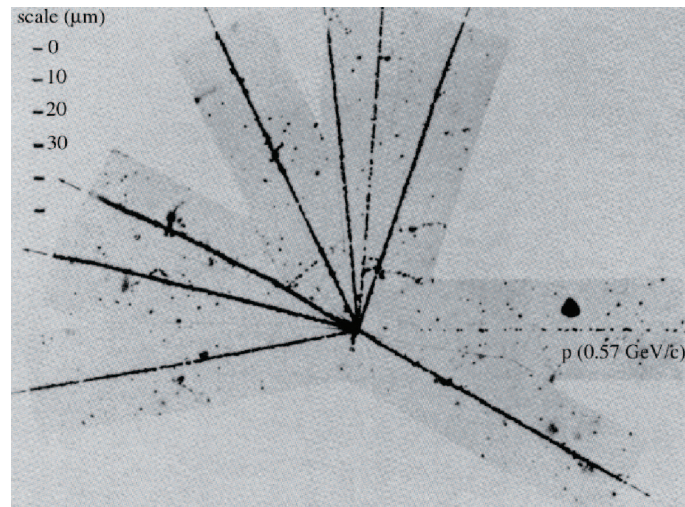


Fig. 12: A nuclear interaction induced by a proton with a kinetic energy of 160 MeV in a nuclear emulsion stack.

As we will see in the next section, very soft shower particles are not only important for the way in which the incoming particle is absorbed, but also for details of the calorimeter response function.

3 The Calorimeter Response Function

3.1 Absolute response and response ratios

I define the *calorimeter response* as the average calorimeter signal per unit of deposited energy. The response is thus expressed in terms of photoelectrons per GeV, pico-coulombs per MeV or something similar. When defined like this, a *linear* calorimeter has a *constant response*.

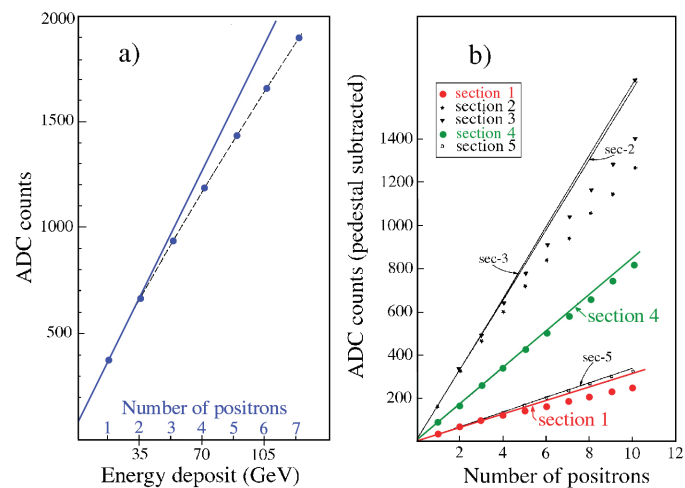


Fig. 13: Average em shower signal from a calorimeter read out with wire chambers operating in the “saturated avalanche” mode, as a function of energy (a). The calorimeter was longitudinally subdivided. Results for the 5 separate sections are given in b [8].

Electromagnetic calorimeters are in general linear, since all the energy carried by the incoming particle is deposited through processes that may generate signals (excitation /ionization of the absorbing medium). Non-linearity is usually an indication of instrumental problems, such as signal saturation or shower leakage. Figure 13 shows an example of a non-linear em calorimeter. In this detector, the wire chambers used to signal the passage of a shower particle operated in the “saturated avalanche” mode, which means that they did not distinguish between 1 and n simultaneous shower particles. As the shower energy, and thus the density of shower particles increased, saturation effects decreased the response. Figure 13b shows that it was the particle *density* and not so much the total energy that was responsible for the effects, since the effects were most prominent early in the shower development (section 1), where the shower was highly collimated. The described effect could be avoided by operating the wire chambers in the proportional regime.

Calorimeters are distinguished according their composition into two classes:

1. *Homogeneous* calorimeters, in which the absorber and the active (signal producing) medium are one and the same.
2. *Sampling* calorimeters, in which these two roles are played by different media.

In the latter instruments, only some fraction of the shower energy is sampled by the active material. This sampling fraction is usually defined on the basis of the signals for *minimum ionizing particles* (mip). For example, in the D0 calorimeter, which consists of 3 mm thick ^{238}U absorber plates separated by 4.6 mm liquid-argon-filled gaps, the sampling fraction for a mip (derived on the basis of the dE/dx values in active and passive material) is 13.7%. However, for em showers, the sampling fraction amounts to only 8.2%.

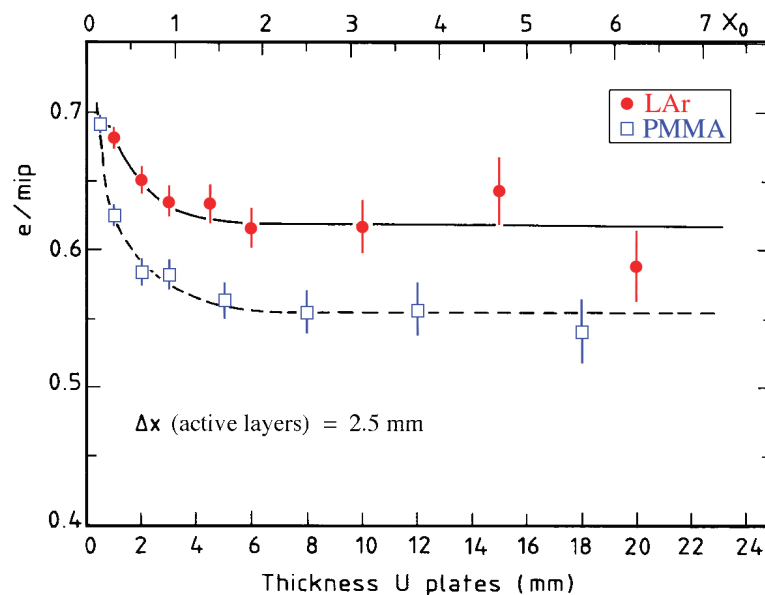


Fig. 14: The e/mip ratio as a function of the thickness of the absorber layers, for uranium/PMMA and uranium/LAr calorimeters. The thickness of the active layers is 2.5 mm in all cases. Results from EGS4 Monte Carlo simulations.

The reason for this difference (we say that this detector has an e/mip response ratio of $8.2/13.7 = 0.6$) is, again, a consequence of the fact that em shower signals are dominated by very soft shower particles. The γ s with energies below 1 MeV are extremely inefficiently sampled in this type of detector, as a result of the overwhelming dominance of the photoelectric effect. Because of the Z^5 cross section dependence, virtually all these soft shower γ s interact in the absorber layers and contributions to the signal may only be

expected if the interaction takes place so close to the boundary with an active layer that the photoelectron (whose range is less than 1 mm) can escape from the absorber into the liquid argon. Because of the crucial role of the photoelectric process, the effect of this phenomenon on the e/mip response ratio depends on the Z values of the passive and active materials (e/mip is smallest for calorimeters with high- Z absorber layers and low- Z active material, as in D0), and on the thickness of the absorber plates (Figure 14). If the latter are made sufficiently thin, e/mip will eventually become 1.0.

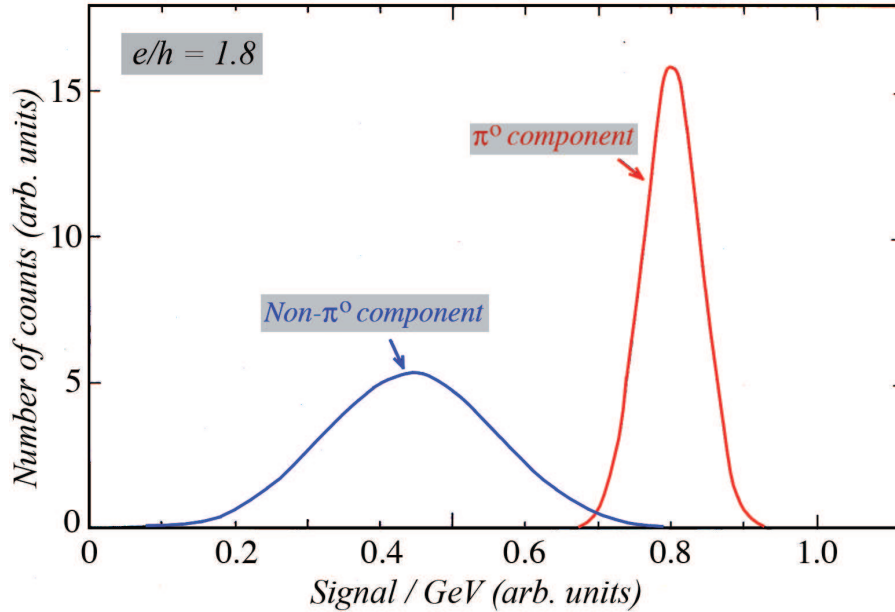


Fig. 15: Schematic representation of the response functions of a non-compensating calorimeter to the em and non-em components of hadronic showers. The ratio of the mean values of these distributions is the e/h value of this calorimeter (1.8).

Signal non-linearity is a very common feature for hadron shower detection. The invisible energy phenomenon and the energy-dependent em shower fraction conspire to this effect, which may easily lead to a response difference of 10% over one order of magnitude in energy. This is schematically illustrated in Figure 15, which depicts the *response function*, *i.e.*, the distribution of the normalized signals around the mean value, separately for the em and non-em components in a non-compensating calorimeter. The ratio of the mean values of these distributions, *i.e.*, the ratio of the em and non-em responses, is known as the e/h value of the calorimeter. In this example, $e/h = 1.8$. A shower induced by a high-energy pion has both an em and a non-em component. The response function of the calorimeter for such pions thus centers around a mean value in between those for the em (e) and non-em (h) components, at a value determined by the average energy sharing between these components at that energy ($\langle f_{em} \rangle$). And since $\langle f_{em} \rangle$ increases with energy (Figure 6), the response to pions increases as well. This calorimeter is thus non-linear for pion detection, its response increases with energy.

The e/h value cannot be directly measured. However, it can be derived from the e/π signal ratios, measured at various energies. The relationship between e/π and e/h is as follows:

$$\frac{e}{\pi} = \frac{e/h}{1 - \langle f_{em} \rangle (1 - e/h)} \quad (2)$$

where $\langle f_{em} \rangle$ represents the (energy-dependent) average em shower fraction. This relationship is graphically illustrated in Figure 16. Even though invisible-energy losses in the non-em component are naturally

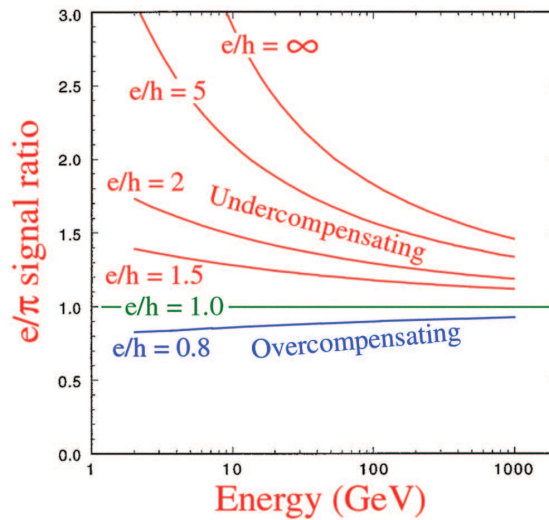


Fig. 16: Relation between the calorimeter response ratio to em and non-em energy deposits, e/h , and the measured e/π signal ratios.

leading to e/h values larger than 1, it turns out to be possible to construct calorimeters with $e/h \leq 1$. Calorimeters with $e/h > 1$, $e/h = 1$ and $e/h < 1$ are called *undercompensating*, *compensating* and *overcompensating*, respectively. Most calorimeters used in practice are undercompensating, with typical e/h values between 1.5 and 2.0.

Equation 2 also quantifies the hadronic signal non-linearity. Since $\langle f_{em} \rangle$ increases with energy, the pion response increases for undercompensating calorimeters, and decreases for overcompensating calorimeters. This is clearly observed in practice (Figure 17). Only compensating calorimeters are linear. This is one of many advantages of compensation.

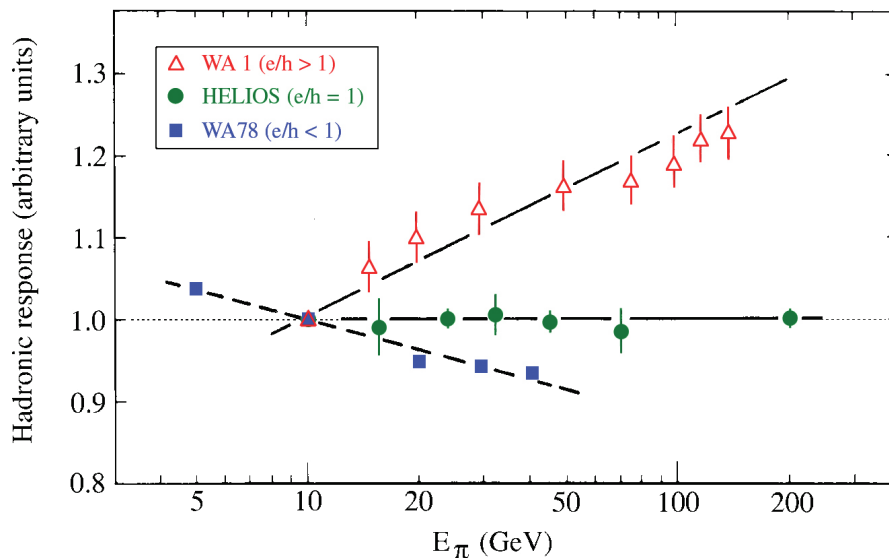


Fig. 17: The response to pions as a function of energy for three calorimeters with different e/h values. All data are normalized to the response for 10 GeV π^- .

3.2 Compensation

In order to understand how compensation can be achieved, one should understand in detail the response to the various types of particles that contribute to the calorimeter signals. Most important in this context are the neutrons. Neutrons carry typically not more than $\sim 10\%$ of the non-em shower energy. However, their contribution to the calorimeter signals may be much larger than that. This is because neutrons only lose their energy through the products of the nuclear reactions they undergo. Most prominent at the low energies typical for hadronic shower neutrons is *elastic scattering*. In this process, the transferred energy fraction is on average

$$f_{\text{elastic}} = \frac{2A}{(A+1)^2} \quad (3)$$

where A is the atomic number of the target nucleus. In hydrogen, this fraction is 50%, in lead it is 100 times smaller. Therefore, MeV-type neutrons sent into a Pb/H₂ structure (50/50 in terms of numbers of nuclei), transfer 98% of their kinetic energy to hydrogen nuclei, and only 2% to lead. Since the sampling fraction for charged particles (mips) amounts to 2.2% in this structure, the potential for *signal amplification through neutron detection* (SAND) is enormous, especially also because the recoil protons produced in the active material may directly contribute to the calorimeter signal.

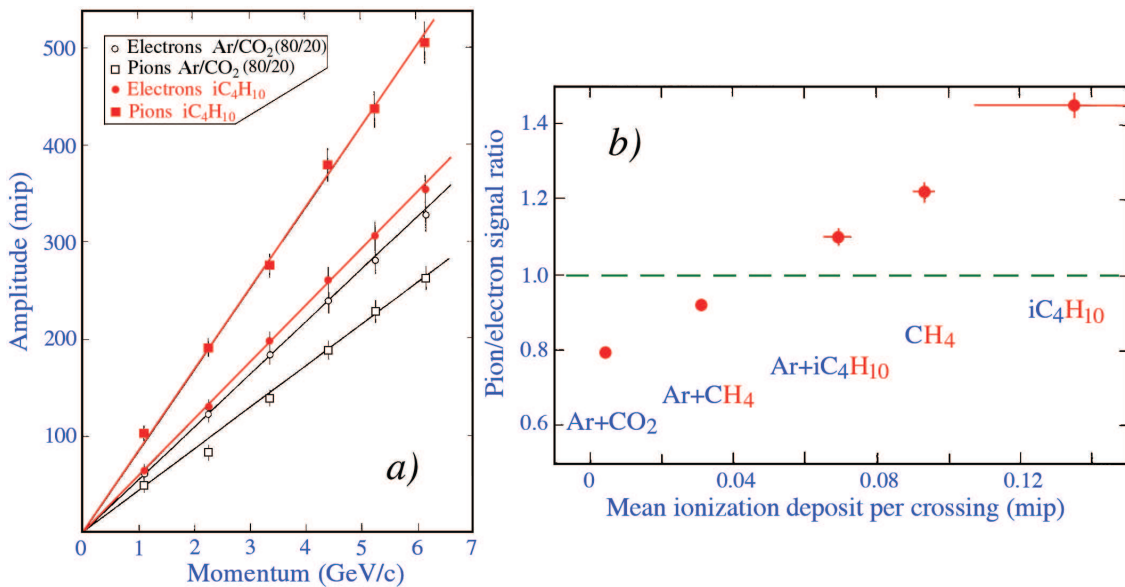


Fig. 18: Signals for pion and electron showers in the L3 uranium/gas calorimeter, for 2 different gas mixtures in the readout chambers (a). Pion/electron response ratio as a function of the hydrogen content of the gas mixture (b).

Hydrogenous active material is an extremely efficient medium for SAND in calorimeters. Nowhere has the role of hydrogen been demonstrated more dramatically than in the L3 uranium/gas calorimeter [10]. Figure 18a shows the signals of this calorimeter for pions and for electrons, as a function of energy, for two different gas mixtures: Argon/CO₂ and isobutane. For the electron signals, the choice of gas made no significant difference. However, the pion response doubled when isobutane (C₄H₁₀) was used instead of argon/CO₂. The L3 group also tested other gas mixtures. It turned out that by changing the hydrogen content of the gas mixture used in the wire chambers that produced the calorimeter signals, the π/e response ratio could be changed by as much as a factor of two. By choosing the proper mixture, the responses to em and hadronic showers could be equalized (Figure 18b).

Compensation can also be achieved in other types of calorimeters, provided that the active material contains hydrogen. By carefully choosing the relative amount of hydrogen in the calorimeter structure, one

can achieve compensation. This has been demonstrated experimentally for plastic-scintillator structures with Pb or ^{238}U as absorber material.

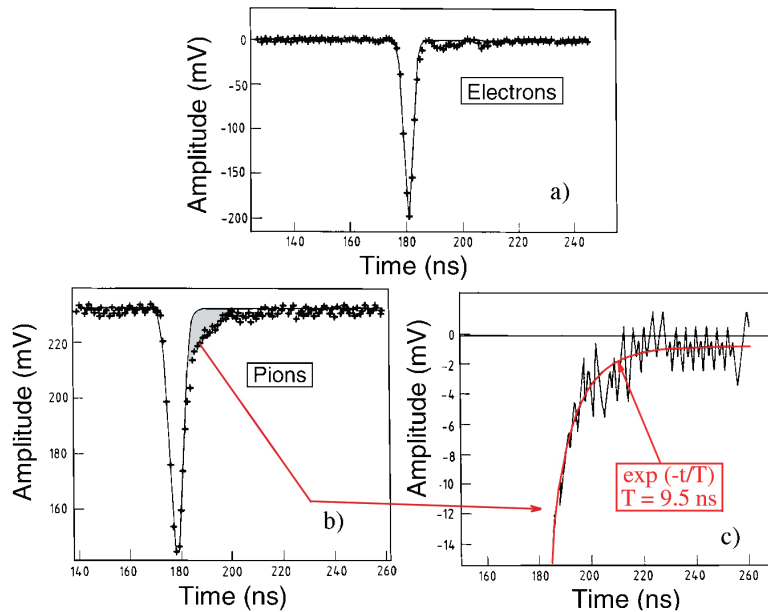


Fig. 19: Typical signals for 150 GeV electrons (a) and pions (b) measured with the SPACAL calorimeter. The pion signal exhibits an exponential tail with a time constant of ~ 10 ns (c).

All compensating calorimeters rely on the contribution of neutrons to the hadronic signals. This is also illustrated by Figure 19, which shows typical time structures of signals recorded with the compensating SPACAL (lead/scintillating plastic fibers) calorimeter [11]. The hadronic signals from this calorimeter (Figure 19b) exhibit a tail which is not seen in the electron signals (Figure 19a). This tail is well described by an exponential with a slope of 10 ns, the characteristic time between subsequent elastic scattering processes of neutrons in this material combination (Figure 19c).

By properly amplifying the neutron signals (with respect to those from charged shower particles depositing the same amount of energy), one can *compensate* for the invisible-energy losses. Therefore, the essential ingredients for a compensating calorimeter are:

- One needs to have a *sampling* calorimeter. Compensation can never be achieved in a homogeneous one.
- The active material needs to contain *hydrogen* and be sensitive to the signals from recoil protons produced by elastic neutron scattering.
- The calorimeter needs to have a precisely tuned *sampling fraction*, in order to amplify the neutron signals by the proper factor. This optimal sampling fraction is $\sim 10\%$ for U/plastic-scintillator (Figure 20) and $\sim 3\%$ for Pb/plastic-scintillator devices.

The use of uranium absorber, for a long time believed to be a key ingredient for compensation, is helpful, but neither essential nor sufficient.

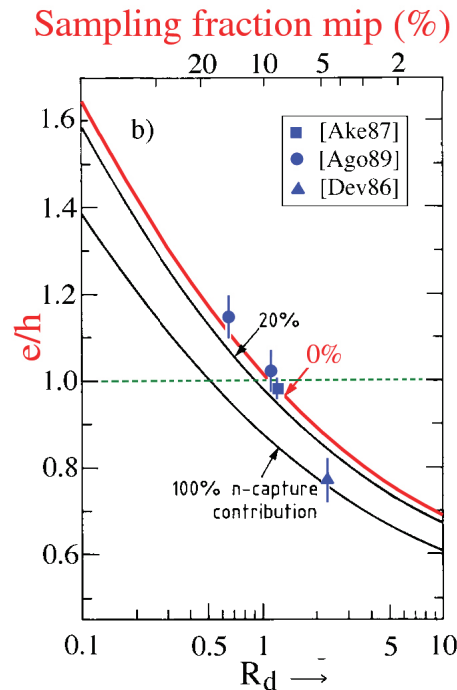


Fig. 20: The e/h ratio of uranium/plastic-scintillator calorimeters as a function of the sampling fraction for mips (top axis) or the volume ratio of passive and active material (R_d , bottom axis). The 3 curves were calculated for different assumptions concerning the contribution of γ s released in thermal neutron capture to the calorimeter signals [9].

3.3 Fluctuations

Since calorimeters are based on physical processes that are inherently statistical in nature, the precision of calorimetric measurements is determined and limited by *fluctuations*. Usually, a variety of fluctuations play a role. In electromagnetic (em) calorimeters, fluctuations that may affect the energy resolution include:

- Signal quantum fluctuations, *e.g.*, photoelectron statistics
- Shower leakage fluctuations
- Fluctuations resulting from instrumental effects, such as electronic noise, light attenuation and structural non-uniformities
- Sampling fluctuations

Only the latter ones are characteristic for sampling calorimeters. In a well designed sampling calorimeter, these fluctuations dominate the others, if that is not the case, then money may have been wasted. Unlike some other fluctuations, *e.g.*, those caused by shower leakage and instrumental effects, sampling fluctuations are governed by the rules of Poisson statistics. Therefore, they contribute to the energy and position resolutions through a term that scales with $1/\sqrt{E}$: $\sigma/E \sim E^{-1/2}$.

Sampling fluctuations are determined both by the sampling fraction (*i.e.*, the relative amount of active material) and the sampling frequency (thickness of the layers). In em calorimeters with non-gaseous active media, they are well described by the following general expression:

$$\frac{\sigma}{E} = 2.7\% \sqrt{d/f_{\text{samp}}} \cdot E^{-1/2} \quad (4)$$

in which d represents the thickness of the active layers (in mm) and f_{samp} is the sampling fraction for mips. For example, in the KLOE lead/scintillating-fiber calorimeter [12], the plastic fibers have a thickness $d = 1.0$ mm. The plastic represents 48% of the detector volume, which otherwise consists of 42% lead and 10% glue. Therefore, the sampling fraction for mips is 15%. Equation 4 thus gives $6.9\%/\sqrt{E}$ as the contribution of sampling fluctuations, in reasonable agreement with the experimental resolution ($5.7\%/\sqrt{E}$).

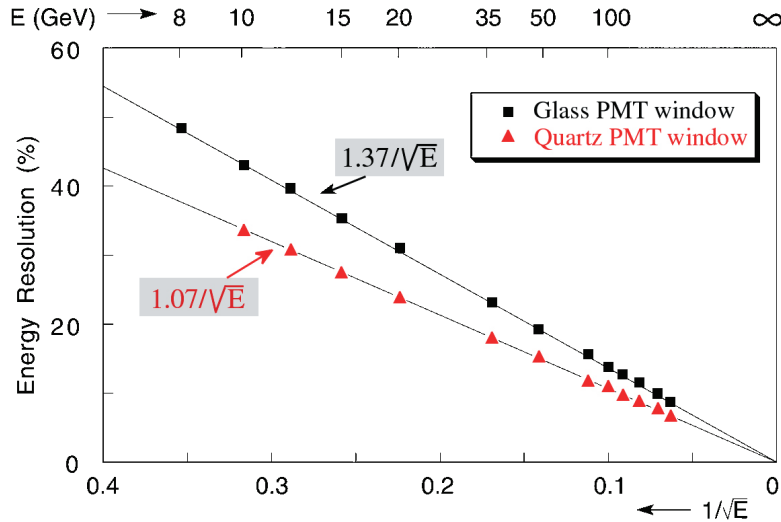


Fig. 21: The energy resolution for electron detection with a CMS/HF prototype detector, as a function of energy. Results are given for measurements in which photomultiplier tubes with a glass window were used and for measurements in which the same type of PMTs were equipped with a quartz window [4].

Among the calorimeters whose resolution is dominated by *signal quantum fluctuations* we mention the Ge detectors used for nuclear γ ray spectroscopy and quartz fiber calorimeters such as the CMS/HF. The amount of energy needed for 1 signal quantum differs by 9 orders of magnitude in these two examples. Whereas it takes only 1 eV to produce an electron-hole pair in germanium, the light yield in quartz fiber calorimeters is typically ~ 1 photoelectron per GeV deposited energy. Signal quantum fluctuations thus limit the resolution of Ge detectors to 0.1% at 1 MeV and of quartz fiber calorimeters to 10% at 100 GeV.

Figure 21 shows the em energy resolution of a CMS/HF prototype as a function of energy. The dominant role of signal quantum fluctuations is illustrated by the fact that by replacing the PMTs which detected the light from this calorimeter by similar PMTs with a quartz window, the resolution improved. This was a direct result of the fact that these quartz windows transmitted a larger fraction of the Čerenkov light that constitutes the signal from this detector.

The effects of (fluctuations in) shower leakage on the em energy resolution of a calorimeter are illustrated in Figure 22. These fluctuations are non-Poissonian and, therefore, their contribution to the energy resolution does not scale with $E^{-1/2}$. It also turns out, that for a given level of shower containment, the effects of longitudinal fluctuations are larger than the effects of lateral fluctuations. These differences are related to the differences in the *number* of different shower particles responsible for the leakage. For example, fluctuations in the starting point of a photon-induced shower translate into leakage fluctuations for which only one particle (the initial photon) is responsible. Side leakage is a collective phenomenon to which typically a large number of shower particles contribute.

Unlike longitudinal and lateral leakage, the third type of leakage, albedo, *i.e.*, backward leakage through the front face of the detector, cannot be affected by the design of the detector. Fortunately, the effects of this type of leakage are usually very small, except at very low energy. The results shown in Figure 22 concern

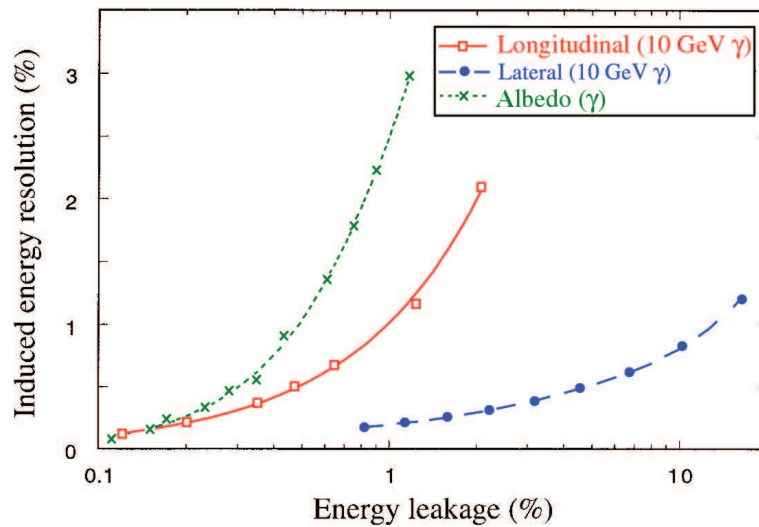


Fig. 22: A comparison of the effects caused by different types of shower leakage. Shown are the induced energy resolutions resulting from albedo, longitudinal and lateral leakage as a function of the energy fraction carried by the particles escaping from the detector. Results from EGS4 Monte Carlo calculations.

Monte Carlo simulations, but have been confirmed by a number of experiments. They hold important lessons for the design of calorimeters (*e.g.*, containment requirements).

In practice, the resolution of a given calorimeter is affected by different types of fluctuations, each with its own characteristic energy dependence. Typically, these effects are uncorrelated and therefore have to be added in quadrature. Because of the different energy dependencies, the total resolution of the calorimeter may be dominated by different effects in different energy regimes.

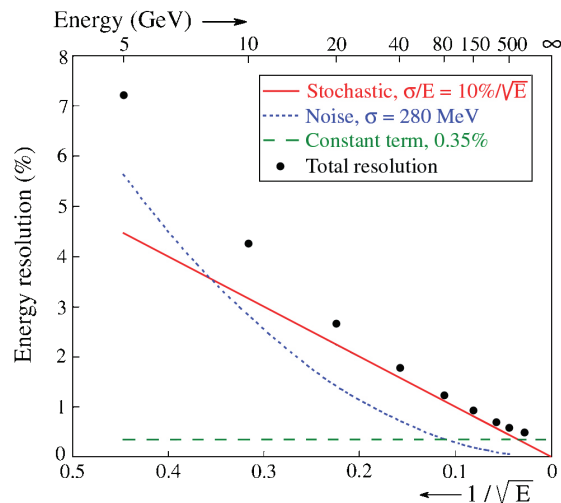


Fig. 23: The em energy resolution and the separate contributions to it, for the ATLAS EM calorimeter [13].

This is illustrated in Figure 23 for the EM calorimeter of the ATLAS experiment. For energies below ~ 10 GeV, electronic noise is the dominating contributor to the resolution, between 10 and 100 GeV sampling

fluctuations and other stochastic terms dominate, while at energies above 100 GeV energy-independent effects (such as the impact-point dependent response) determine the resolution.

The same factors listed above also affect the resolution for hadron detection. Sampling fluctuations are larger for hadron showers than for em ones, typically by a factor of two. This is due to the fact that the hadronic shower signals are dominated by the contributions from spallation protons, which typically carry a few hundred MeV of energy. Unlike the Compton and photo-electrons that dominate the signals from em showers, these spallation protons may traverse several active calorimeter layers. Also, their specific ionization is larger than for mips. Therefore, the number of *different* shower particles that contribute to the calorimeter signals is smaller for hadron showers. Fluctuations in this number, which are the dominating source of sampling fluctuations, are thus larger for hadron showers than for em showers developing in the same detector.

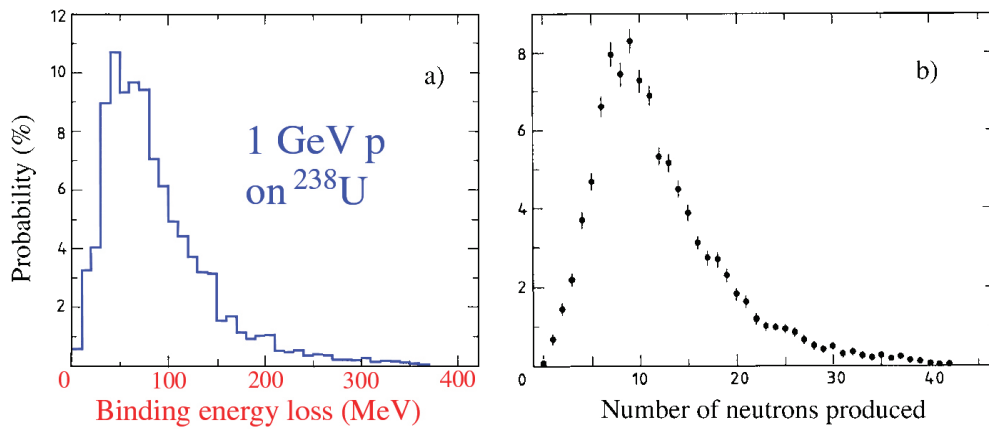


Fig. 24: The nuclear binding energy lost in spallation reactions induced by 1 GeV protons on ^{238}U nuclei (a), and the number of neutrons produced in such reactions (b).

However, there are some additional effects that tend to dominate the performance of hadron calorimeters. In the nuclear reactions through which many hadrons are absorbed, some fraction of the energy is used to release nucleons from nuclei. This binding energy is *invisible*, it does not contribute to the calorimeter signals. Fluctuations in visible energy play a role in *all* hadron calorimeters and form the ultimate limit to the achievable hadronic energy resolution. Figure 24 gives an impression of these fluctuations [9].

In *non-compensating* calorimeters, which respond differently to the em and non-em shower components ($e/h \neq 1$), the *non-Poissonian* fluctuations in the em shower fraction (f_{em}) tend to dominate the hadronic performance. These fluctuations contribute to the energy resolution *not* through a constant term as is often thought, but rather through an energy-dependent term, $cE^{-0.28}$, which has to be added in quadrature to the other contributing terms, with the parameter c determined by the e/h value ($0 < c < 1$). The result resembles the solid line in Figure 25 which, in the energy range accessible to measurements, runs almost parallel to the curve representing the results of a calorimeter in which only a stochastic term (scaling with $E^{-1/2}$) plays a role. For this reason, one sees the hadronic energy resolution of non-compensating calorimeters sometimes expressed as

$$\frac{\sigma}{E} = \frac{a_1}{\sqrt{E}} + b \quad (5)$$

instead of

$$\frac{\sigma}{E} = \frac{a_2}{\sqrt{E}} \oplus cE^{-0.28} \quad (6)$$

Note that the values of a_1 and a_2 in this comparison are different (Figure 25).

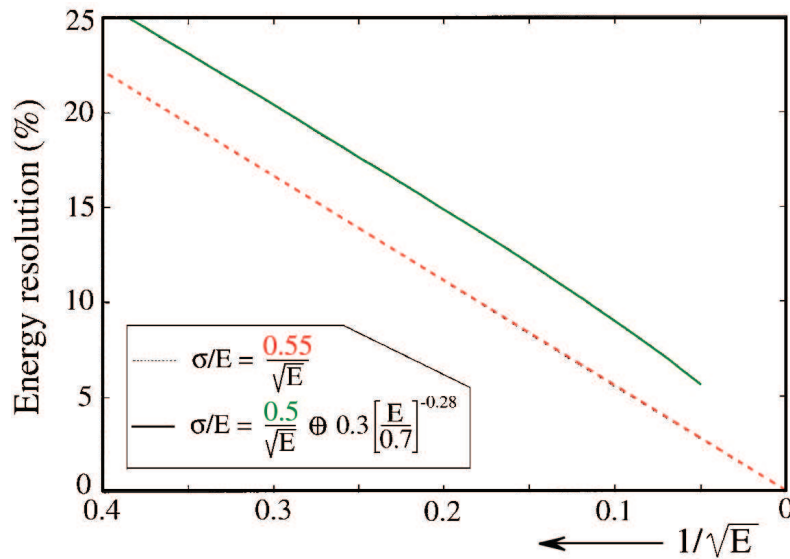


Fig. 25: The hadronic energy resolution calculated for a typical non-compensating calorimeter in the energy regime up to 400 GeV (the solid line), and calculated with a sole stochastic term with a slightly larger scaling constant [1].

The resolution of compensating calorimeters is ultimately limited by fluctuations in (in)visible energy. The importance of these fluctuations depends on the details of how compensation is achieved. In plastic-scintillator calorimeters, the signal from neutrons is correlated with the nuclear binding energy losses, especially for high- Z absorber material. Therefore, the intrinsic fluctuations are reduced. However, this effect is stronger in lead than in uranium, where many neutrons come from fission processes and thus are unrelated to the nuclear binding energy losses. As a result, the ultimate energy resolution achievable with Pb-based calorimeters is better than for uranium ones: $13\%/\sqrt{E}$ vs. $20\%/\sqrt{E}$ [14].

3.4 The shape of the response function

Not all types of fluctuation give rise to response variations that are symmetric about the average value. Examples of effects that lead to an asymmetric response function include, but are not limited to the following.

- If the signal is constituted by a very small number of signal quanta (*e.g.*, photoelectrons), then the Poisson distribution becomes asymmetric. Effects of this type have been observed in the signals from quartz-fiber calorimeters (Figure 26).
- Effects of shower leakage lead to tails in the signal distributions. Usually, these tails occur on the low-energy side of the signal distribution, since energy is escaping from the active detector volume. However, there are examples of detectors where leakage leads to signal amplification, for example in scintillating calorimeters read out by silicon diodes, where an escaping shower electron may produce a signal in the diode that is orders of magnitude larger than that produced by a scintillation photon (Figure 27a).
- An interesting effect occurs in non-compensating hadron calorimeters. As we saw earlier, fluctuations in the energy fraction spent on π^0 production (f_{em}) dominate the resolution of such devices. However, these fluctuations are not necessarily symmetric. For example, in showers induced by pions, the probability of an anomalously large f_{em} value is not equal to that of an equivalently small value. The reason for that is the *leading-particle effect*. A large f_{em} value occurs when in the first nuclear interaction a large fraction of the energy carried by the incoming pion is transferred to a π^0 . However,

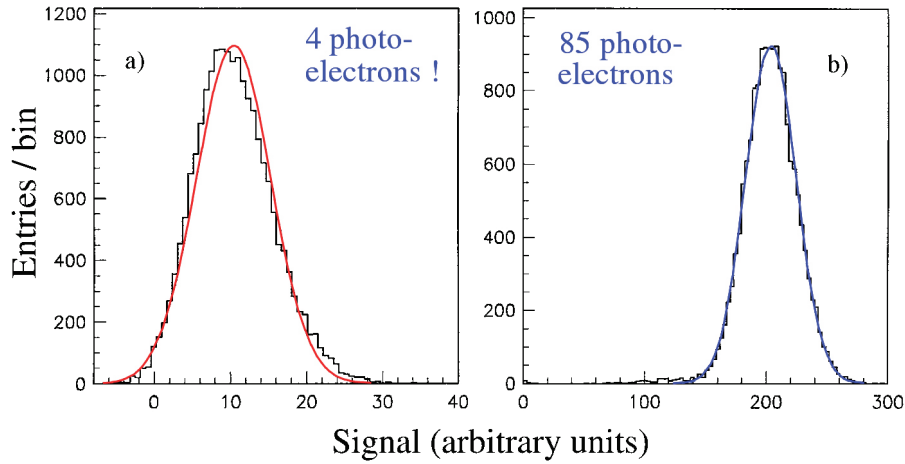


Fig. 26: Signal distributions for 10 GeV (a) and 200 GeV (b) electrons showering in the CMS Quartz-Fiber Calorimeter. The curves represent Gaussian fits to the experimental data [4].

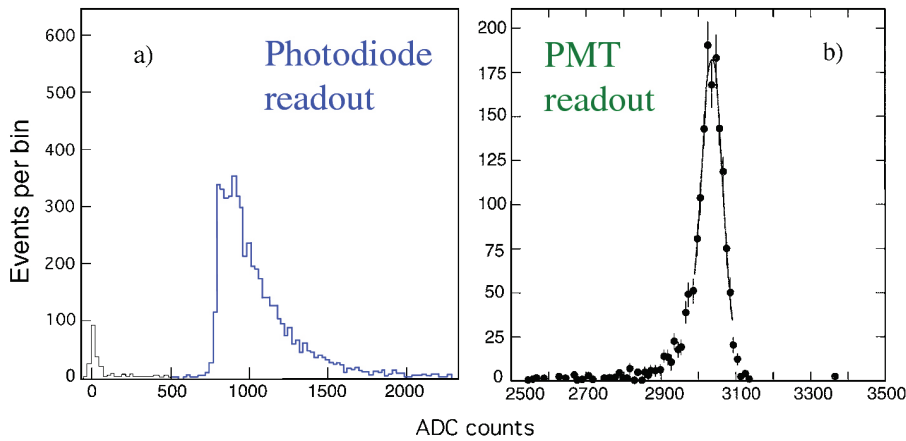


Fig. 27: Signal distributions for high-energy electron showers measured with a PbWO_4 crystal calorimeter [15]. The calorimeter was read out either with silicon photodiodes (a) or with PMTs (b).

when a similarly large fraction is transferred to another type of particle, the result is not necessarily a small f_{em} value, since this other particle may produce energetic π^0 s in subsequent reactions. This effect leads to significant differences in the signal distributions for showers induced by high-energy pions and protons (Figure 28). In proton-induced showers, the leading particle has to be a baryon and asymmetries such as the ones discussed above are absent.

It is important to note that the response function observed for pion-induced showers is not only determined by the asymmetric fluctuations in f_{em} , but also by the e/h value of the calorimeter. For example, in compensating calorimeters, the response function for pions is perfectly Gaussian, despite the asymmetric fluctuations in f_{em} . On the other hand, in overcompensating calorimeters, the asymmetry in the response function is reversed (*i.e.*, a low-side tail is observed). These features can be understood from the schematic representation shown in Figure 15. If $h > e$, then an excess of events with an anomalously large f_{em} value will manifest itself as an excess of events with an anomalously *small* total signal.

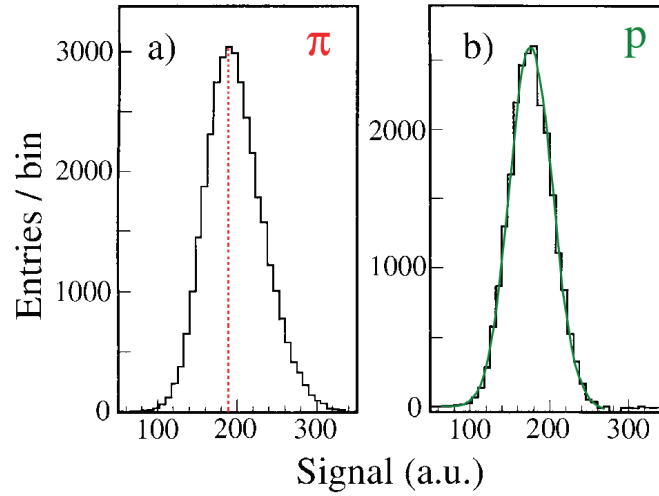


Fig. 28: Signal distributions for 300 GeV pions and protons detected with a quartz-fiber calorimeter. The curve in (b) represents the result of a Gaussian fit to the proton distribution [16].

3.5 Lessons for calorimeter design

There are some important lessons to be drawn from the characteristics discussed on the previous pages:

- Usually, a variety of different types of fluctuations contribute to the energy resolution of a calorimeter. However, one of these sources of fluctuations dominates. If one wants to improve the calorimeter's energy resolution, one has to work on the fluctuations that *dominate*. As an example, I mention the fact that one has built at some point a *homogeneous* calorimeter for hadron detection, consisting of 60 tons of liquid scintillator. In this device, all sources of fluctuation were eliminated (by design), except

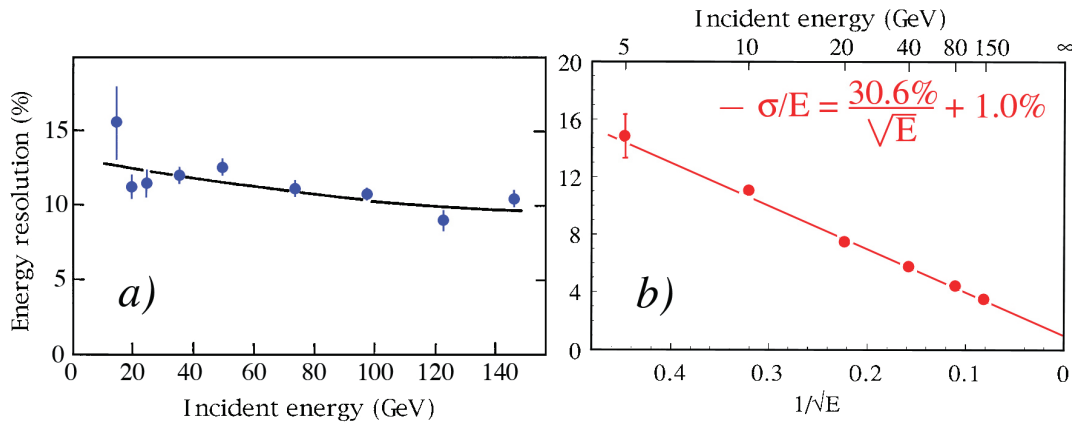


Fig. 29: The hadronic energy resolution as a function of energy, for a homogeneous calorimeter consisting of 60 tonnes of liquid scintillator (a), and for the compensating SPACAL calorimeter, which has a sampling fraction of only 2% (b). From Reference [17].

for the effects of non-compensation. The resolution of this device was limited to 10% (Figure 29a). On the other hand, the SPACAL detector, a sampling calorimeter designed to eliminate the effects of non-compensation, achieved hadronic energy resolutions of $\sim 2\%$ at high energy (Figure 29b).

In the design of a calorimeter, one should not waste money reducing fluctuations that do not dominate the performance. Unfortunately, this lesson is not always followed in practice. A few examples may illustrate this:

- A thin ($< 2\lambda_{\text{int}}$ deep) calorimeter intended for detecting high-energy ($> 10^{11}$ eV) cosmic rays (mainly protons) outside the Earth's atmosphere is subject to severe effects of shower leakage. These effects completely dominate the energy resolution. Therefore, a high-quality crystal (BGO) is as good as a crudely sampling device in this respect, if neither is capable of measuring the effects of shower leakage event-by-event [33].
- A calorimeter system with a crystal em section, chosen for ultimate performance in detecting em showers, will have poor performance for hadron detection, *no matter what* one chooses for the hadronic section. The large e/h value of the em section, combined with the large event-to-event fluctuations in the energy sharing between both sections spoils the hadronic performance of the detector. An example of this is shown in Figure 30, and concerns the CMS experiment at CERN's Large

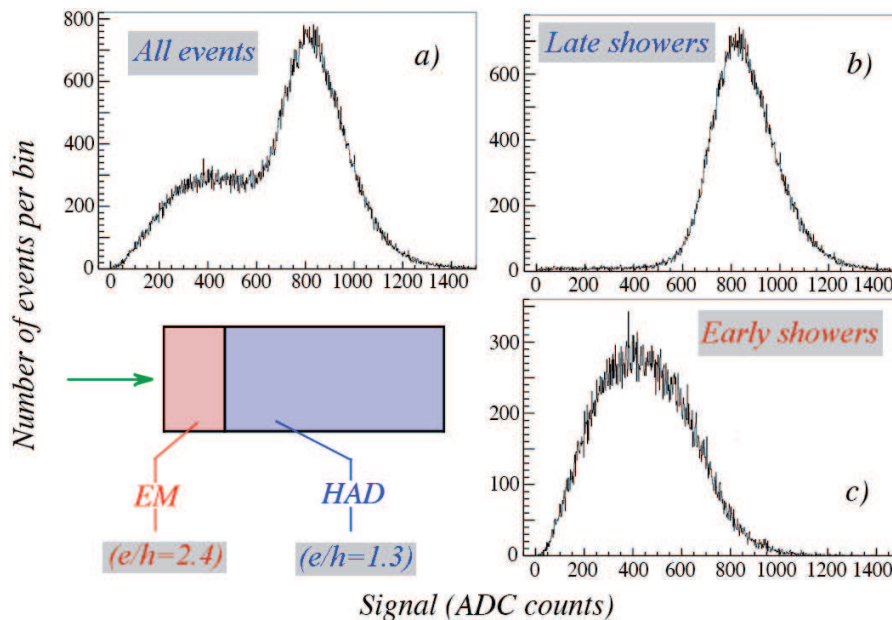


Fig. 30: Signal distributions for 10 GeV pions showering in the CMS calorimeter system. Events in which the pions penetrate the crystal em section and deposit all their energy in the hadronic section (b) have a very different signal distribution than events in which the shower starts in the em section (c). The total signal distribution (a) is a superposition of the two.

Hadron Collider. The CMS calorimeter system is optimized for em shower detection, with a PbWO_4 crystal em section. The large e/h value of this section (2.4) has spectacular effects for hadrons. The figure shows very different signal distributions for 10 GeV pions, depending on the starting point of the showers. In practice, this starting point cannot always be determined, especially if these pions are part of a collimated jet. If that is the case, the response function is given by Figure 30a.

- The light yield of quartz-fiber detectors is typically so small that signal quantum fluctuations (photoelectron statistics) are a major contributing factor to the energy resolution. If that is the case, there is nothing to be gained from increasing the sampling frequency, *i.e.*, by using more, thinner fibers instead of fewer, thick ones.

4 Calibration and Simulation

4.1 Calibration

Calibration, *i.e.*, establishing the relationship between deposited energy and the resulting calorimeter signals is perhaps the most important, and also the most underestimated, aspect of working with a calorimeter system. In Section 2, we saw that the performance of calorimeters is determined by processes that take place in the last stages of the shower development. This feature has also important consequences for the calibration of longitudinally segmented devices.

In em showers developing in a sampling calorimeter, the sampling fraction for soft γ s is different from that for mips. Therefore, the overall sampling fraction of the calorimeter is a function of depth, or shower age. This is illustrated in Figure 31. This effect does not only depend on the Z values of active and passive

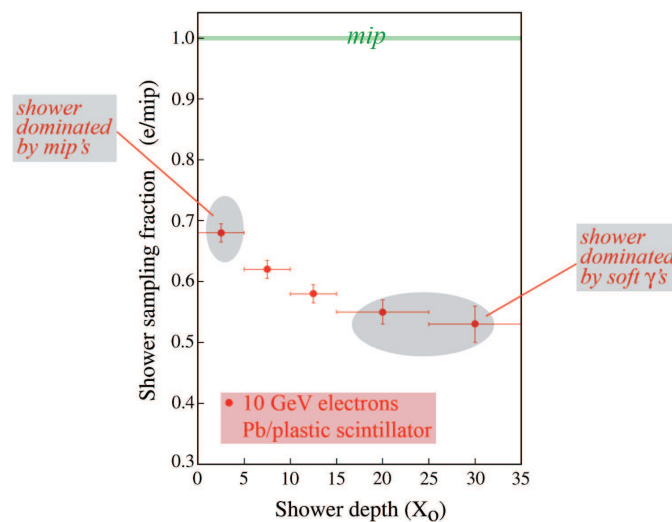


Fig. 31: The e/mip ratio as a function of the shower depth, or age, for 1 GeV electrons in various sampling calorimeter configurations. All calorimeters consisted of $1X_0$ thick absorber layers, interleaved with 2.5 mm plastic scintillator. Results from EGS4 Monte Carlo simulations.

material, but also on the shower energy. The lower the shower energy, the earlier soft shower particles from Compton scattering and photoelectric effect will dominate. If the calorimeter is longitudinally segmented, then the ratio between deposited energy and resulting calorimeter signal is different for the different segments. As a result, the energy deposited in these different segments is systematically mismeasured, in an energy dependent way. This is illustrated in Figure 32, which shows the extent of this mismeasurement for the two sections constituting the HELIOS calorimeter [18]. The energy in the first ($6.6X_0$ deep) section is systematically overestimated, the energy in the second segment is systematically underestimated, when the scintillator signals are considered a measure for the deposited energy.

In practice, one has to define calibration constants for these two sections and the question arises how these have to be chosen. Almost all methods that are used in practice are wrong. For example, HELIOS exploited a method in which the calibration constants were chosen such that the total width of the signals was minimized, as illustrated in Figure 33.

However, the values of the calibration constants A and B , and in particular also the ratio B/A , were found to depend on the energy of the electrons that were used to calibrate the detector. This is illustrated in Figure 34a and is a direct consequence of the effects discussed above (Figures 31,32). In particular, the value of B/A was found to differ from 1, *i.e.*, the value found when both sections are intercalibrated with muons, which are sampled by both sections in exactly the same way. It turned out that this calibration method (for em showers in a compensating calorimeter!) led to

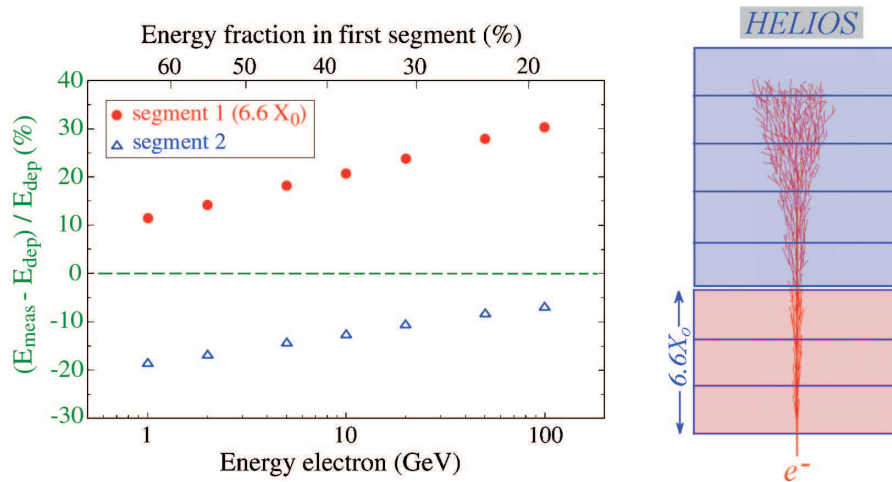


Fig. 32: Fractional mismeasurement of the energy deposited in the individual sections of the longitudinally segmented HELIOS U/plastic-scintillator calorimeter, as a function of the energy of the showering electrons (*bottom axis*) or the energy sharing between the two calorimeter sections (*top axis*).

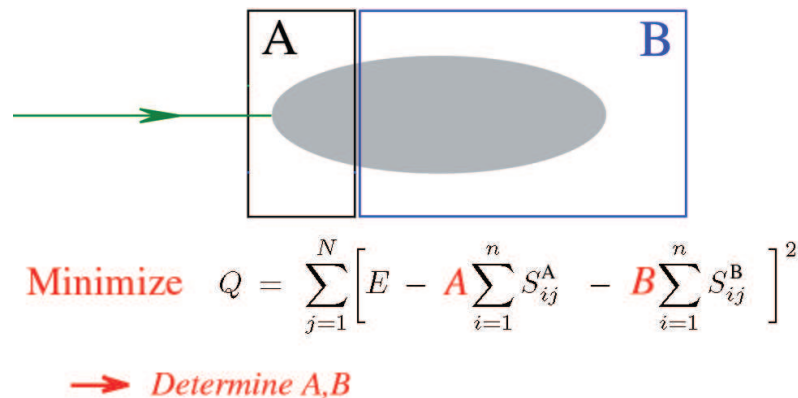


Fig. 33: Intercalibration of the sections of a longitudinally segmented calorimeter with showers that share their energy between these sections.

- energy-dependent calibration constants,
- em response non-linearities, and
- systematic differences between the responses to electrons, γ s and π^0 s (Figure 34b).

All these effects are well documented and understood [2, 19]. The effects are even worse for hadrons and non-compensating calorimeters. In that case, almost all methods used in practice lead to a dependence of the reconstructed energy on the starting point of the shower, and to systematic mismeasurement of the energy of jets (collections of simultaneously showering particles). Also here, several methods that are widely used in practice have undesirable side effects.

As an example, we mention a method illustrated in Figure 35 which is used in several experiments, *e.g.*, CDF. In this method, each section of the longitudinally segmented calorimeter is calibrated with particles that deposit their entire shower energy in that particular section. Electrons are used to calibrate the EM section, and the hadronic section is calibrated with pions that penetrate the em section without

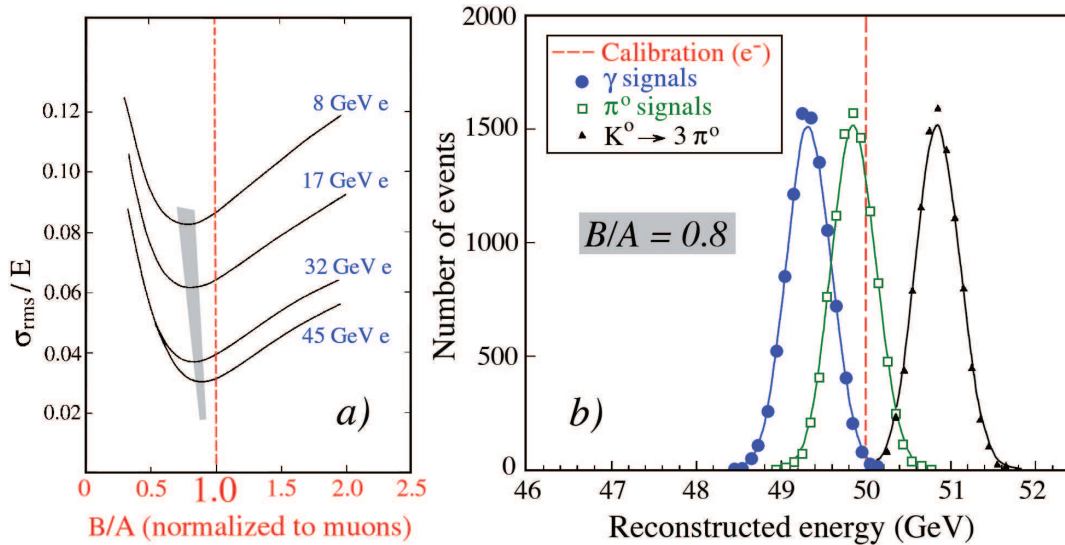


Fig. 34: The fractional width σ/E of the signal distributions for electrons of different energies, as a function of the intercalibration constant B/A of the HELIOS calorimeter system. The dashed line corresponds to the intercalibration constant derived from muon measurements (a). Signal distributions for γ s and for hadrons decaying into all- γ final states. All particles have the same nominal energy and the detector, which has an intrinsic resolution of 0.5% for em showers of this energy, was calibrated with electrons using $B/A = 0.8$ (b).

undergoing a nuclear interaction and start a shower in the hadronic section. Although this method at first sight looks quite reasonable, it leads to major problems. The vast majority of the hadrons, and

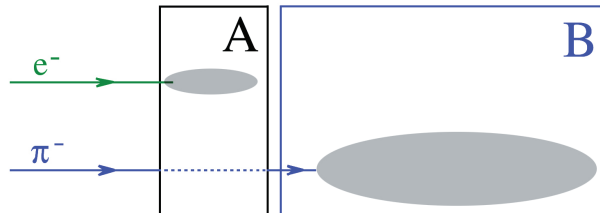


Fig. 35: Calibration of a longitudinally segmented calorimeter with different types of particles which deposit all their energy in one of the segments.

all the jets, do **not** penetrate the EM section without depositing a significant fraction of their energy. Typically, about half of the energy is deposited in the EM section (with large event-to-event fluctuations in the percentage) and if the standard calibration constant of that section is used, the energy of the hadrons and jets is systematically underestimated (if $e/h > 1$), to an extent depending on the energy sharing and on the e/h value of the calorimeter.

This is illustrated in Figure 36, where the merits of this method were studied with 350 GeV pions in a testbeam setting. Shown are total signal distributions for events in which different fractions of the (unweighted) shower energy were recorded in the EM section of a longitudinally segmented quartz-fiber calorimeter. The fraction was compatible to zero (a), 10-20% (b), or 60-80% (c). The average total calorimeter signal is shown as a function of this fraction in diagram d. The calorimeter was calibrated on the basis of $B/A = 1.51$ in all these cases, as required for reconstructing the energy of 350 GeV pions that penetrated the EM compartment without undergoing a strong interaction. The figure shows that for all other

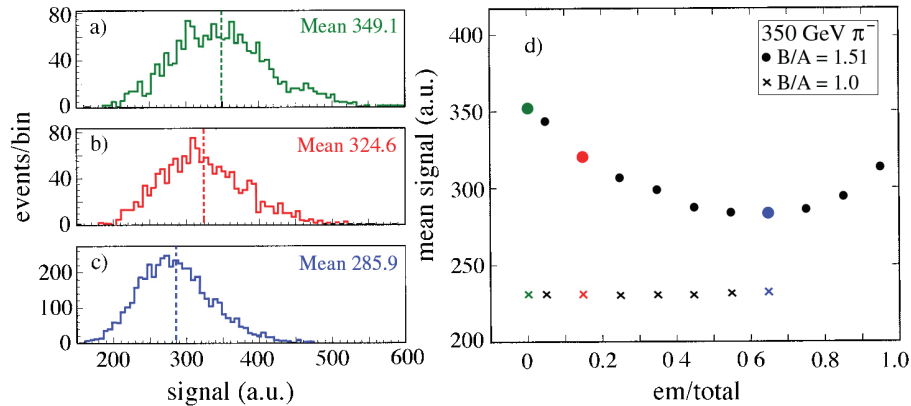


Fig. 36: Signal distributions for 350 GeV pion showers in a longitudinally segmented quartz-fiber calorimeter, for events in which different fractions of the (unweighted) shower energy were recorded in the em calorimeter section (a, b, c). The average calorimeter signal for 350 GeV pions, as a function of this fraction, is shown in diagram d.

events, the total energy is *underestimated*, in some cases by as much as 20%! [19]. Diagram d also contains results (the crosses) obtained for a calibration on the basis of $B/A = 1$. In that case, the reconstructed energy does *not* depend on the sharing between the two calorimeter compartments. However, because of the non-compensating nature, the reconstructed energy is too small, but always by the same fraction. If the e/h value of the calorimeter system is known, the latter effect can be corrected for, by means of an energy-dependent factor.

In the above example, the different calorimeter sections had exactly the same structure, and thus the same e/h value. In practice, this is likely not to be true, in which case one will face additional problems. An example of such a system is the CMS calorimeter, which consists of a crystal em section ($e/h = 2.4$), followed by a brass/plastic-scintillator hadronic section ($e/h = 1.3$). The response of this detector to electrons and pions is shown as a function of energy in Figure 37 [20]. Because of the large difference between the e/h values of the two sections, the response to pions strongly depends on the starting point of the shower, even when both sections are calibrated in the same way (with electrons in this case). The resulting signal distributions are shown in Figure 30. If one does not know the starting point of the shower, as is usually the case when the pion is part of a collimated jet, one has no choice but to use the average response. Fortunately, a jet consists typically of a large number of particles, and the effects of using the average are much reduced for the *jet response*.

The measurements shown in Figure 37 cover a large range of energies (1 - 300 GeV) and are therefore very important for understanding several other calorimetric issues as well. Among these, we mention the large non-linearity effects, especially at low energy and large e/h , differences between the response to different types of hadrons (π, p, \bar{p}), and the fact that the hadronic response tends to increase at very low energy (< 3 GeV), where an increasing fraction of the particles stop in the calorimeter without inducing nuclear reactions and therefore don't suffer signal-reducing invisible-energy losses.

Apart from CMS, there are many other calorimeter systems where longitudinal segmentation is the cause of major calibration problems. As an example, we mention the AMS experiment [21]. This lead/scintillating-fiber calorimeter is subdivided into 18 longitudinal segments of $\sim 1X_0$ each. Each of these segments was calibrated with mips, and the energy equivalent of a mip traversing one segment was established to be 11.7 MeV. However, the total depth of this calorimeter ($17X_0$) is not sufficient to fully contain high-energy electron showers, as can be seen in Figure 38a. As a result, the total signal is not proportional to the beam energy. The larger the beam energy, the larger the fraction that leaks out (Figure 38b). The authors tried to compensate for this effect by fitting the measured signals in the 18 segments to a standard shower profile. By integrating this profile to infinity, they expected to determine the average

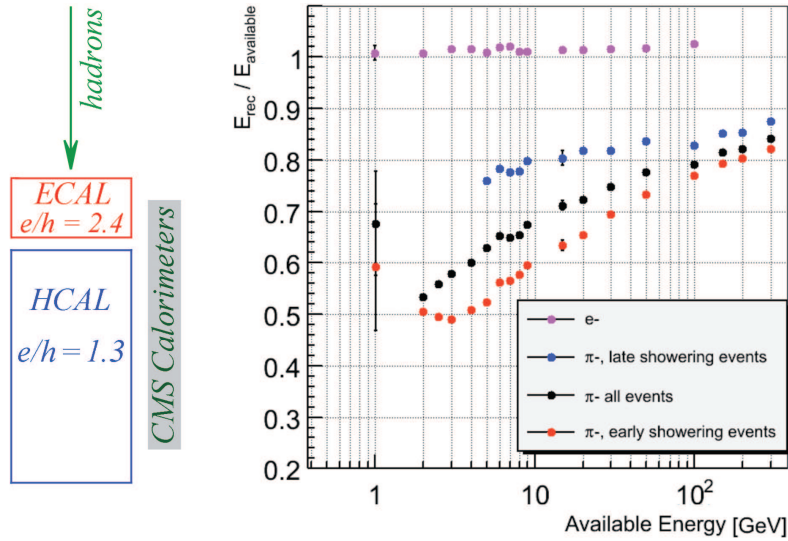


Fig. 37: The response to pions as a function of energy, for the CMS barrel calorimeter system [20]. Both the em ($PbWO_4$ crystals) and hadronic (brass/scintillator) sections were calibrated with electrons. The events were subdivided into two samples according to the starting point of the shower: in the em or the hadronic section. Results are given for these two samples, as well as for the overall data sample.

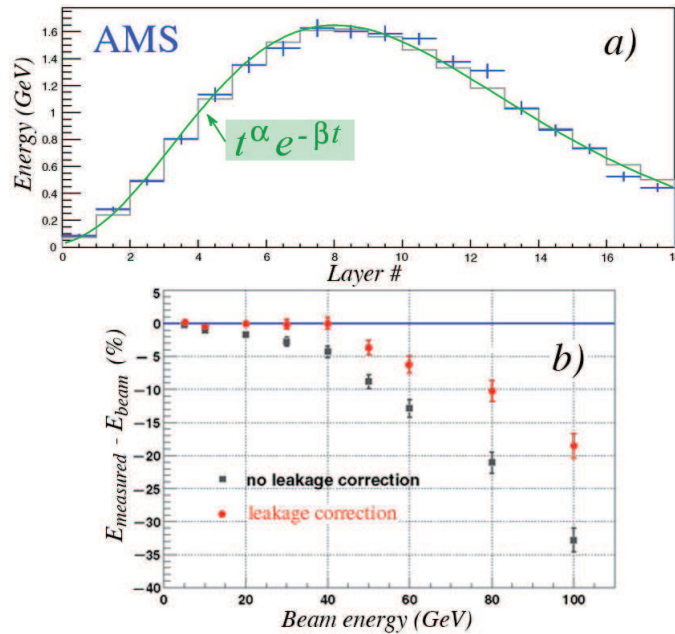


Fig. 38: Average signals for 100 GeV electron showers in the 18 longitudinal sections of the AMS lead/scintillating-fiber calorimeter (a). Average difference between the measured energy and the beam energy, before and after leakage corrections based on extrapolation of the fitted shower profile (b).

shower leakage. However, as illustrated by the circles in Figure 38b, this method only led to a partial recovery of the missing energy. This can be understood from the fact that the measured signals beyond the shower maximum corresponded to a significantly larger energy than the signals from the early part of the

shower development (Figure 31). By using the same signal-to-energy conversion throughout the module, the energy leaking out the back is thus systematically underestimated. Therefore, the reconstructed shower energy is systematically too small, more so if the leakage fraction is larger.

One approach that has produced reasonable results in practice comes from the ATLAS Collaboration. Their Pb/LAr ECAL consists of 3 longitudinal segments ($4.3X_0$, $16X_0$ and $2.0X_0$ deep, respectively). Also in this detector, the sampling fractions decrease considerably with depth, despite the uniform detector structure. The calibration constants were determined on the basis of detailed Monte Carlo simulations, which were optimized such as to achieve simultaneously good energy resolution and signal linearity [22]. The reconstructed energy was derived from the measured signals with a formula that contains at least 4 parameters which depend in a non-linear way on the energy of the incoming electrons. With this formula, the authors achieved excellent linearity for the energy range 15 - 180 GeV. Impressive as these results may be, one has to realize that the parameter values are only valid for one particular pseudorapidity, and that the parameter values will also have to be different when the signals are produced by photons instead of electrons. It is also unclear how these results extend beyond the energy range for which they were obtained: at 10 GeV, a very significant deviation from linearity was observed. The ATLAS and CMS examples illustrate that life will not be easy at the LHC, if one wants to achieve the advertised calorimeter performance in practice.

In conclusion, I would like to say that it is important to keep in mind that calibration should first and foremost lead to (on average) correct reconstruction of the energy of the showering particle. This condition is distinctly different from requirements concerning the width of a signal distribution, signal linearity or other desirable features that often form the basis of the chosen calibration scheme [19, 23]. In my opinion, given the disadvantages, longitudinal calorimeter segmentation should be avoided as much as possible. There is nothing that can be achieved thanks to longitudinal segmentation that cannot be achieved (better) in other ways. To illustrate the latter statement, Figure 39 shows how one can distinguish signals produced

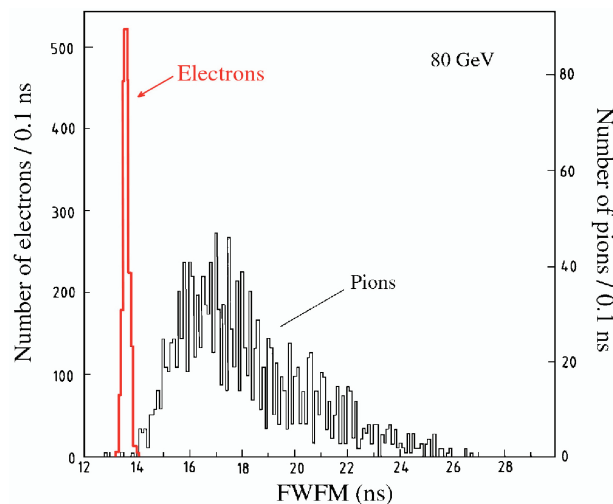


Fig. 39: Particle identification in a longitudinally unsegmented calorimeter.

by em and hadronic showers in a longitudinally unsegmented calorimeter, simply on the basis of the time structure of the signals. The figure shows the width of the pulses, measured at 20% of the amplitude, in a lead/plastic-scintillating fiber calorimeter [11]. This type of particle identification has traditionally been one of the arguments to separate the calorimeter system into em and hadronic sections. Figure 39 is only of many examples that illustrate that this can also be achieved in non-segmented calorimeters.

4.2 Monte Carlo simulations

In the past decade, the importance of Monte Carlo (MC) simulations in particle physics has grown very fast. In practice, almost every experimental result is confronted with its MC equivalent, MC techniques are being used to correct experimental results for detector imperfections, such as limited acceptance, and entire experiments are designed in detail on the basis of MC simulations. In the previous section, we also gave an example in which calibration constants are derived on the basis of MC simulations.

However, it is important to realize that a Monte Carlo program is only as good as the physics on which it is based. Unfortunately, Monte Carlo simulations of hadronic shower development, and in particular those available in the GEANT package, are seriously flawed in this respect. As a result, Monte Carlo simulations of hadronic calorimeter performance have little or no predictive value, especially for what concerns performance characteristics that are very sensitive to a correct implementation of these physics processes, *e.g.*, hadronic energy resolutions, e/π signal ratios and hadronic response functions.

In the past 15 years, tremendous progress has been made in our fundamental understanding of hadron calorimetry and of the subtleties of the physics processes that make compensation possible. However, none of this has been achieved as a result of “full GEANT simulations”. It is even fair to say that this progress was made *in spite of* such simulations, given the importance that many people attach to them (“if GEANT does not describe your experimental data, there must be something wrong with the data”).

The situation is quite different for em showers, where the availability of a highly reliable Monte Carlo code (EGS4) has greatly contributed to a deeper understanding of a variety of important issues, such as the mechanisms that lead to $e/mip \neq 1$ in sampling calorimeters, the problems encountered when intercalibrating the sections of longitudinally segmented calorimeters with em showers, *etc.*

It is extremely important that simulation programs be developed that have the same degree of reliability for hadron showers as EGS4 has for em showers. To reach that goal, it is useful to define a series of “benchmark” calorimeter results that can be used to gauge the quality of the simulation programs, and to measure the progress achieved in this domain.

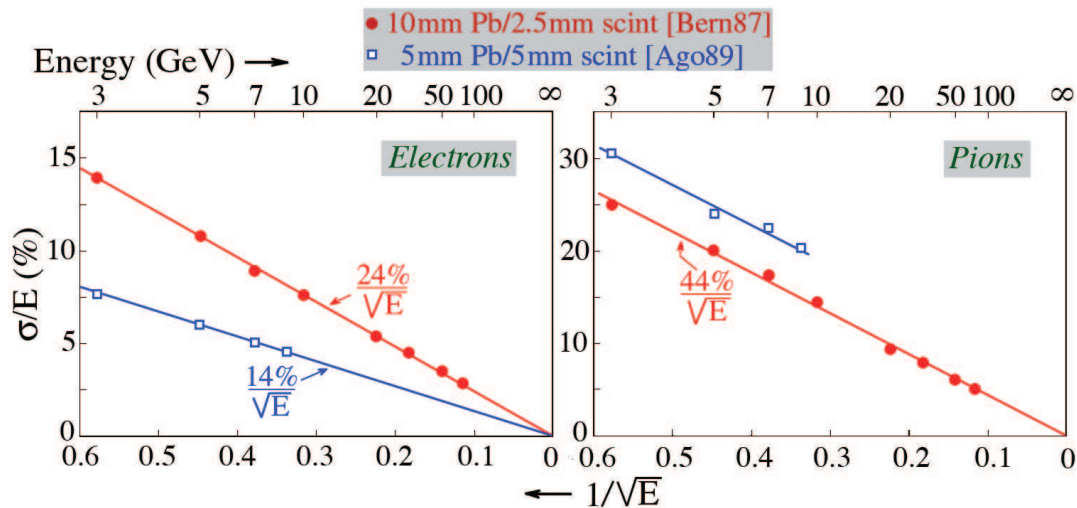


Fig. 40: Calorimeter benchmark data for testing the correct implementation of soft neutron scattering in Monte Carlo simulations of hadronic shower development. See text for details.

The most sensitive tests of the correctness of hadronic shower simulation programs are provided by calorimeters in which one particular aspect of the shower development is strongly emphasized. As an example, I mention lead/plastic-scintillator calorimeters built in the framework of the ZEUS prototype studies [24,25]. The signals from such calorimeters are strongly affected by evaporation neutrons produced

in the showers. Data from such calorimeters are thus particularly suited for testing that particular aspect of the simulations.

Figure 40 shows the energy resolutions for electrons and pions measured with two of these lead/plastic-scintillator calorimeters. The sampling fractions of these calorimeters differed by a factor of four. The data from the fine-sampling calorimeter are represented by the open squares, the closed circles correspond to the data from the cruder sampling device. Not surprisingly, the em resolution of the fine-sampling calorimeter is better, by about a factor of two. However, the resolution for pions is clearly better for the cruder sampling detector. As the energy increases, the difference becomes more pronounced, since the resolution of the crude sampling detector scales with $E^{-1/2}$, while the other one does not. The e/h value of the crude sampling calorimeter was measured to be 1.05 ± 0.04 , while for the other detector, e/π signal ratios between 1.3 and 1.4 were reported for energies in the energy range 3–8.75 GeV. No “full GEANT simulation” has ever managed to describe these experimental data, or other benchmark data that emphasize other aspects of hadronic shower development, *e.g.*, the differences between pion- and proton-induced showers in non-compensating calorimeters (see Figure 28), which are a sensitive probe of how well effects related to π^0 production in showers are described. Therefore, further development of our understanding of calorimetry will have to proceed as it has in the past 15 years, *i.e.*, without any meaningful input or feedback from “full GEANT” simulations.

5 The Future of Calorimetry

The energy resolution achievable with crystal calorimeters, based on materials such as CsI(Tl) or BGO, is unrivaled at em shower energies below ~ 20 GeV. However, one should realize that below 1% the resolution is determined by factors other than the intrinsic stochastic term of the detector. Instrumental effects tend to dominate at that point. For this reason, excellent resolution is not a unique feature of crystals at energies above 20 GeV. Sampling calorimeters such as those used in the KLOE [12] and NA48 [26] experiments offer comparable performance. At energies above 50 GeV, crystals offer no specific advantage over other, much cheaper types of detectors. Crystals are substantially less ideal in calorimeter systems with which one also wants to detect hadrons or jets. The latter are collections of photons and hadrons, the result of fragmenting quarks, diquarks or gluons. The effects of the large e/h values of crystal calorimeters were discussed before and illustrated in Figures 30 and 37.

In general, factors other than the calorimeter resolution also play an important role in jet detection, in particular the jet algorithm and contributions of underlying events to the signals. However, as the energy increases and jets become more collimated, these effects become relatively less important. Especially at a high-energy linear e^+e^- collider, there is no reason why one should not aim to measure the fourvectors of *all* elementary constituents of matter (including quarks and gluons) with a precision of $\sim 1\%$.

It has become customary to express the energy resolution of calorimeters as the quadratic sum of a scaling term and an energy independent (“*constant*”) term:

$$\frac{\sigma}{E} = \frac{c_1}{\sqrt{E}} \oplus c_2 \quad (7)$$

and often the performance of actual devices is referred to in terms of the value of c_1 . As we have seen in Section 3.3, this parameterization is **fundamentally incorrect**, especially for hadronic showers in non-compensating calorimeters. Therefore, I propose to quote the resolution in terms of a fraction at a given energy, or in terms of the value of σ at that energy. And, of course, σ should represent the *rms* value of the signal distribution, not the result of a Gaussian fit that ignores the non-Gaussian tails characteristic of the signals from non-compensating calorimeters.

An often quoted design criterion for calorimeters at a future high-energy linear e^+e^- collider is the need to distinguish between hadronically decaying W and Z bosons, and it is claimed that c_1 has to be smaller than 0.3 (30%) to achieve that. This means that one should be able to detect 80-90 GeV jets with a

resolution of 3 - 3.5 GeV. This goal can be achieved with compensating calorimeters. However, because of the small sampling fraction required for compensation, the em energy resolution is limited in such devices (e.g., $15\%/\sqrt{E}$ [27]). Also, because of the crucial role of neutrons produced in the shower development, the signals would have to be integrated over relatively large volumes and time intervals to achieve this resolution, which is not always possible in practice. In the following, we discuss some other methods that are currently being pursued to circumvent these limitations.

5.1 The Energy Flow Method

One method that has been proposed in this context, the so-called *Energy Flow Method*, is based on the combined use of a precision tracker and a highly-granular calorimeter. The idea is that charged jet fragments can be precisely measured with the tracker, while the energy of the neutral particles is measured with the calorimeter. Such methods have indeed successfully been used to improve the resolution of jets from Z^0 decay at LEP, to ~ 7 GeV [28].

The problem that limits the success of this method is of course that the calorimeter does not know or care whether the particles it absorbs are electrically charged. Therefore, one will have to correct the calorimeter signals for the contributions of the charged jet fragments.

Proponents of this method have advocated a fine granularity as the key to the solution of this “double-counting” problem [29]. However, it has been argued that, for practical geometries, this is an illusion [30]. Especially in jets with leading charged fragments, the overlap between the showers from individual jet fragments makes the fine granularity largely irrelevant. In the absence of energy constraints, such as the ones used at LEP, the proposed method may improve the performance of a poor calorimeter system by $\sim 30\%$, but the resolution gets nowhere near the performance one may expect from a dedicated stand-alone calorimeter system [30].

Of course, in the absence of any reliable Monte Carlo simulations, the only way to prove or disprove the advocated merits of the proposed method is by means of dedicated experiments in realistic prototype detectors. To that end, the CALICE Collaboration has built an impressive instrument [31], containing $\sim 14,000$ electronic readout channels. However, experimental results from several years of testbeam operations have not (yet) provided any evidence that the mentioned performance requirements can be met with this approach.

5.2 Off-line compensation

The energy resolution of a calorimeter is determined by *fluctuations*, not by mean values. This means that one should not expect any beneficial effect from methods in which the signals from different calorimeter sections are weighted by different factors in an attempt to equalize the response to electromagnetic and hadronic showers. Such methods are known as “offline compensation techniques”.

This statement may be illustrated by an example taken from practice. Figure 41 shows test results obtained with a non-compensating calorimeter that was preceded by various amounts of “dead” material (iron). This iron had a larger absorbing effect on electron showers than on hadronic ones. As a result, the e/π signal ratio measured with the calorimeter decreased as the amount of iron was increased (Figure 41a). For an absorber thickness of $8X_0$ (13 cm Fe), the compensation condition $e/\pi = 1$ was achieved. Yet, the hadronic energy resolution was significantly worse than without the “dummy” iron section (Figure 41b). This is of course no surprise, since the signals were collected from only part of the block of matter in which the shower develops. Fluctuations in the fraction of the energy deposited in the part from which the signals were collected added to the ones that determined the resolution in the absence of the dummy section and thus deteriorated the resolution.

Although this is maybe a somewhat extreme example, it does illustrate the fact that there is no magic in the e/π signal ratio. The resolution of a non-compensating calorimeter is determined by the event-to-event fluctuations in the em shower content and as long as nothing is done to reduce (the effect of) these

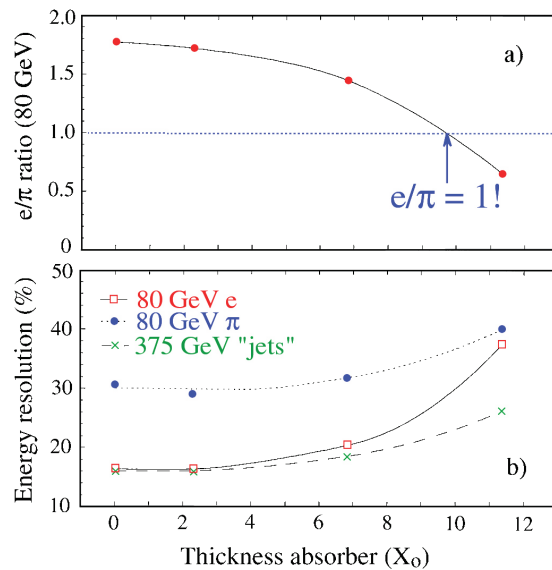


Fig. 41: The e/π signal ratio at 80 GeV (a) and the energy resolution (b) of a non-compensating calorimeter preceded by dead material (iron), as a function of the thickness of this material. The energy resolution is given for 80 GeV electrons and pions, as well as for 375 GeV multiparticle "jets" generated by 375 GeV pions in an upstream target [32].

fluctuations *event by event*, no improvement in the hadronic energy resolution may be expected. The

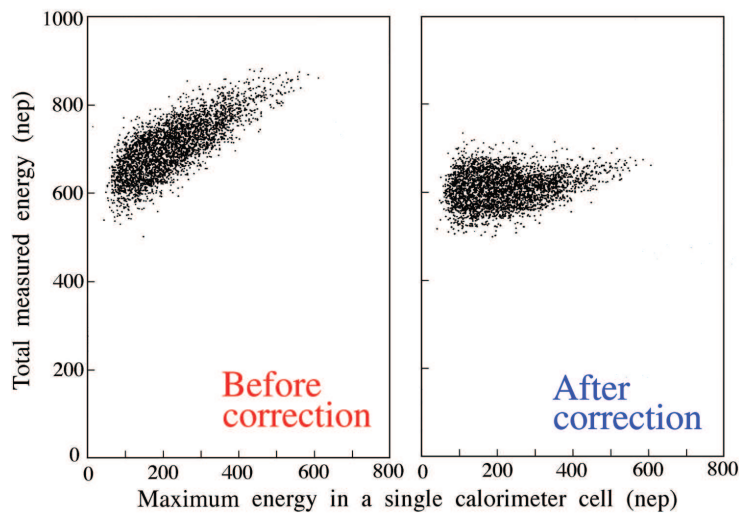


Fig. 42: WA1 results on off-line compensation, showing the correlation between the total measured signal and the maximum signal observed in one individual calorimeter segment. Results are given for 140 GeV pions before and after applying a weighting factor, based on the signals observed in the individual calorimeter segments [6].

key for possible success of such weighting methods lies thus in the *event-by-event* aspect. There are some examples in the literature of more or less successful attempts to improve the hadronic energy resolution through a determination of the em shower content event by event (*e.g.*, Figure 42). These methods were all based on the different spatial dimensions of the em and non-em shower components. The em showers

develop in a much smaller detector volume and thus lead to local areas of high energy deposit density (see also Figure 7). Such methods work reasonably well in a clean testbeam environment for single particles carrying a precisely known energy. However, when confronted with a collection of particles of unknown composition and energies (jets), their benefit is much less clear.

5.3 Dual-readout calorimetry

An alternative approach to measuring the em shower fraction (f_{em}) event by event, which does not rely upon the spatial shower characteristics, exploits the fact that the production of Čerenkov light in hadron showers is almost exclusively due to the em shower component. This is a result of the fact that the electrons and positrons through which the em shower energy is deposited are relativistic down to ~ 0.2 MeV, while the spallation protons that dominate the non-em calorimeter signals are typically non-relativistic (see Section 2). Therefore, by comparing the amounts of Čerenkov light and scintillation light produced by a hadron shower, one can determine the em shower fraction event by event.

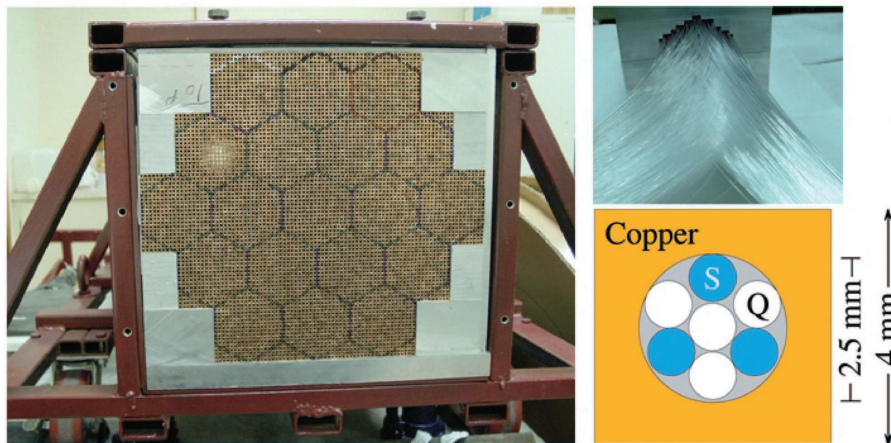


Fig. 43: Layout of the DREAM calorimeter. The basic element is a 200 cm long extruded copper tube (cross section 4×4 mm², with a central hole of 2.5 mm diameter. Three scintillating fibers and 4 undoped Čerenkov fibers are inserted in this hole. The calorimeter consists of about 6000 such tubes. The fibers are split as they exit at the rear into bunches of the two types of fibers.

The value of this method was first demonstrated with an instrument intended to measure high-energy (PeV) cosmic hadrons. This $1.4 \lambda_{int}$ deep calorimeter was equipped with 2 types of optical fibers, plastic-scintillator and quartz, which measured the scintillation and Čerenkov light, respectively [33]. The ratio of the quartz and scintillator signals turned out to be a good event-to-event measure for the fraction of the shower energy carried by π^0 s produced in the first interaction, and thus for the shower leakage, which dominated the resolution of this thin detector. Inspired by this success, a fully-containing ($10 \lambda_{int}$ deep) calorimeter was built and tested. This instrument and the Collaboration that operates it became known as DREAM (Dual-REAdout Method). Some results are shown below [34, 35].

The basic element of the detector (Figure 43) is a hollow, extruded copper tube, 200 cm long and 4×4 mm² in cross section. Seven optical fibers are inserted in the 2.5 mm wide hole, 3 scintillating fibers and 4 clear ones for detecting Čerenkov light. The detector consists of about 6000 such tubes and contains in total ~ 90 km of fibers. The fibers are split as they exit at the rear into bunches of the two types of fibers. In this way, a hexagonal readout structure is created. Each hexagonal cell is read out by 2 PMTs, one for each type of light. Figure 44 shows the signal distributions for 100 GeV π^- recorded in this device. The signal distributions are asymmetric, reflecting the characteristics of the f_{em} fluctuations. The central value

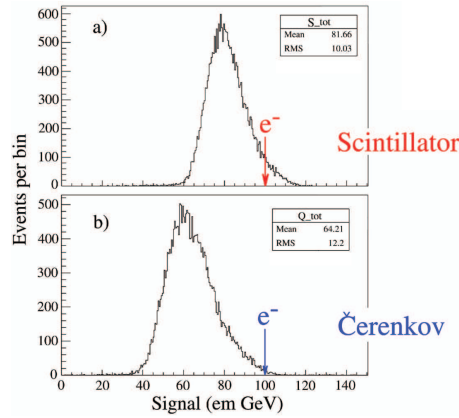


Fig. 44: Signal distributions for 100 GeV π^- recorded by the scintillating (a) and the Čerenkov (b) fibers. The signals are expressed in the same units as those for em showers, which were used to calibrate the detector.

is also considerably smaller than that for the electrons that were used to calibrate the detector, by 18% and 36% for the scintillator and Čerenkov signals, respectively.

Using the ratio of the two signals, the value of f_{em} could be determined *event-by-event* in a straight-

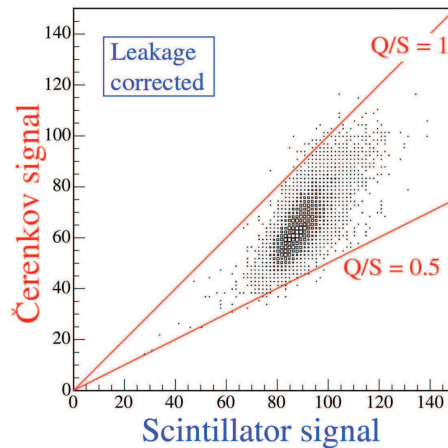


Fig. 45: Čerenkov signals versus scintillator signals, for 100 GeV π^- in DREAM.

forward way. The value of this ratio (Q/S) is represented by a straight line in the scatter plot of the two signals (Figure 45). This ratio is related to the em shower fraction as

$$\frac{Q}{S} = \frac{f_{em} + 0.21(1 - f_{em})}{f_{em} + 0.77(1 - f_{em})} \quad (8)$$

where 0.21 and 0.77 represent the h/e ratios of the Čerenkov and scintillator calorimeter structures, respectively. The merits of this method are clearly illustrated by Figure 46, which shows the overall Čerenkov signal distribution for 100 GeV π^- (a), as well as distributions for subsamples selected on the basis of their f_{em} value (b), determined by Equation 8. Each f_{em} bin probes a certain region of the overall signal distribution, and the average value of the subsample distribution increases with f_{em} .

Once the value of f_{em} was determined, the signals could be corrected in a straightforward way for the effects of non-compensation. In this process, the energy resolution improved, the signal distribution

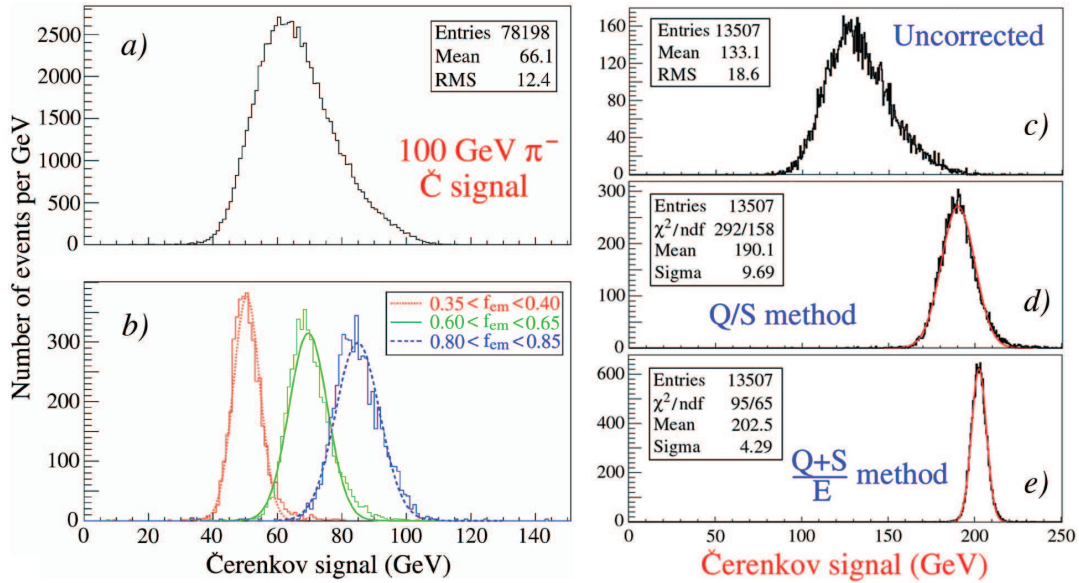


Fig. 46: Čerenkov signal distribution for 100 GeV π^- (a) and distributions for subsamples of events selected on the basis of the measured f_{em} value, using the Q/S method (b). Signal distributions for high-multiplicity “jets” in the DREAM before (c) and after (d) corrections on the basis of the observed Čerenkov/scintillator signal ratio were applied. In diagram e, energy constraints were used, which eliminated the effects of lateral shower fluctuations that dominate the resolution in d.

became much more Gaussian and, most importantly, the hadronic energy was correctly reproduced. This was true both for single pions as well as for jets, an important difference with the methods based on the energy deposit profile, which do not work for jets.

The results for 200 GeV “jets” are shown in Figure 46c-e. These “jets” were in fact not fragmenting quarks or gluons, but multiparticle events created by pions interacting in a target placed upstream of the calorimeter. Using only the *ratio* of the two signals produced by this calorimeter, the resolution for these “jets” was improved from 14% to 5%, in the Čerenkov channel. It was shown that this 5% resolution was in fact dominated by fluctuations in side leakage in this (small, only 1200 kg instrumented volume) detector. Eliminating such fluctuations led to a further considerable improvement (Figure 46e).

Also the jet energy was well reconstructed as a result of this procedure (Figure 47). Whereas the raw data gave a mean value of 133.1 GeV for these 200 GeV jets, the described procedure led to hadronic energies that were within a few percent correct, *in an instrument calibrated with electrons*. In the process, hadronic signal linearity (a notorious problem for non-compensating calorimeters) was more or less restored as well. Any remaining effects can be ascribed to side leakage and would most likely be eliminated in a larger detector of this type.

Simultaneous detection of the scintillation and Čerenkov light produced in the shower development turned out to have other, unforeseen beneficial aspects as well. One such effect is illustrated in Figure 48, which shows the signals from muons traversing the DREAM calorimeter along the fiber direction. The gradual increase of the response with the muon energy is a result of the increased contribution of radiative energy loss (Bremsstrahlung) to the signals. The Čerenkov fibers are *only* sensitive to this energy loss component, since the primary Čerenkov radiation emitted by the muons falls outside the numerical aperture of the fibers. The constant (energy-independent) difference between the total signals observed in the scintillating and Čerenkov fibers represents the non-radiative component of the muon’s energy loss. Since both types of fibers were calibrated with em showers, their response to the radiative component is

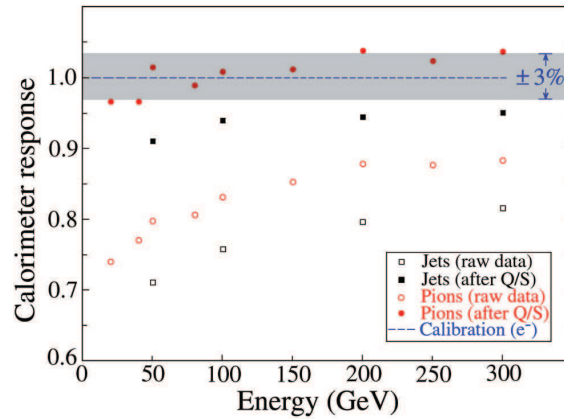


Fig. 47: The DREAM response to single pions and high-multiplicity jets, before and after corrections made on the basis of the measured Čerenkov/scintillator signal ratio.

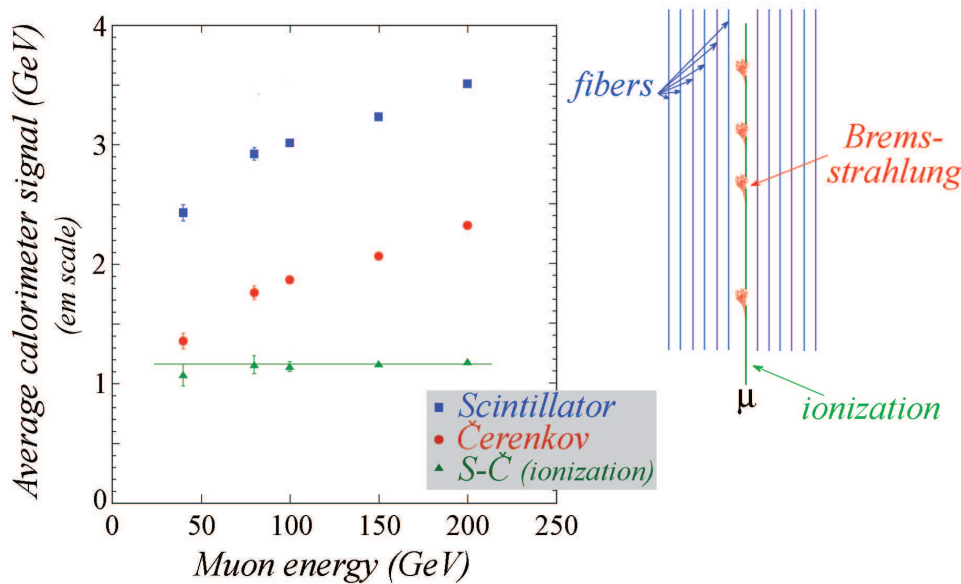


Fig. 48: Average values of the scintillator and Čerenkov signals from muons traversing the DREAM calorimeter, as a function of the muon energy. Also shown is the difference between these signals. All values are expressed in units of GeV, as determined by the electron calibration of the calorimeter [34].

equal. This is the only example I know of a detector that separates the energy loss by muons into radiative and non-radiative components.

Once the effects of the dominant source of fluctuations are eliminated, the resolution is determined and limited by other types of fluctuations. In the case of the DREAM detector, these fluctuations include, apart from fluctuations in side leakage which can be eliminated by making the detector larger (see Figure 46e), *sampling fluctuations* and fluctuations in the Čerenkov light yield. The latter effect alone (8 Čerenkov photoelectrons per GeV) contributed $35\%/\sqrt{E}$ to the measured resolution. The DREAM Collaboration is currently exploring the possibilities to use crystals for dual-readout purposes. Certain dense high- Z crystals (PbWO_4 , BGO) produce significant amounts of Čerenkov light, which can in principle be separated from the scintillation light by exploiting differences in time structure, spectral properties and

directionality. This offers the possibility to obtain further significant improvements of the DREAM results. Other improvements may come from event-by-event measurements of the contribution of neutrons to the calorimeter signals, *e.g.*, from the time structure of the signals.

6 Outlook

We have come a long way in improving calorimeters from rather crude instrumented absorbers to precision detectors. The key to these improvements has always come from a better understanding of the shower development process and its translation into calorimeter signals. Monte Carlo simulations have provided little or no guidance, especially in hadron calorimetry. Trial and error has been and remains the method of choice. Therefore, the only way to further this process is generic detector R&D. We have certainly not yet reached the end of the road in that respect. I believe this field is potentially full of interesting projects for graduate students and postdocs. Moreover, time and effort invested in this field is likely to pay off, since a better understanding of the detectors is key to a full exploitation of the physics potential of the experiment in which the detectors are to be used.

References

- [1] Wigmans R 2000, *Calorimetry, Energy Measurement in Particle Physics*, International Series of Monographs on Physics, Vol. 107, Oxford University Press (2000).
- [2] Wigmans R and Zeyrek M 2002, Nucl. Instr. and Meth. **A485**, 385.
- [3] Acosta D *et al.* 1992, Nucl. Instr. and Meth. **A316**, 184.
- [4] Akchurin N *et al.* 1997, Nucl. Instr. and Meth. **A399**, 202.
- [5] Green D 1994, *Proc. 4th Int. Conf. on Calorimetry in High Energy Physics*, La Biodola, Italy, eds. A. Menzione and A. Scribano, (Singapore: World Scientific), p. 1.
- [6] Abramowicz H *et al.* 1981, Nucl. Instr. and Meth. **180**, 429.
- [7] Acosta D *et al.* 1990, Nucl. Instr. and Meth. **A294**, 193.
- [8] Atač M *et al.* 1983, Nucl. Instr. and Meth. **205**, 113.
- [9] Wigmans R 1987, Nucl. Instr. and Meth. **A259**, 389.
- [10] Galaktionov Y *et al.* 1986, Nucl. Instr. and Meth. **A251**, 258.
- [11] Acosta D *et al.* 1991, Nucl. Instr. and Meth. **A302**, 36.
- [12] Antonelli A *et al.* 1995, Nucl. Instr. and Meth. **A354**, 352.
- [13] Gingrich D *et al.* 1995, Nucl. Instr. and Meth. **A364**, 290.
- [14] Drews G *et al.* 1990, Nucl. Instr. and Meth. **A290**, 335.
- [15] Peigneux JP *et al.* 1996, Nucl. Instr. and Meth. **A378**, 410.
- [16] Akchurin N *et al.* 1998, Nucl. Instr. and Meth. **A408**, 380.
- [17] Wigmans R 1998, Rev. Sci. Instr. **69**, 3723.
- [18] Åkesson T *et al.* 1987, Nucl. Instr. and Meth. **A262**, 243.
- [19] Ganel O and Wigmans R 1998, Nucl. Instr. and Meth. **A409**, 621.
- [20] Akchurin N *et al.* 2007, *The Response of the CMS Combined Calorimeters to Single Hadrons, Electrons and Muons*, CMS Note 2007/012, CERN, Gen'ève, Switzerland.
- [21] AMS Collaboraion 2002, Nucl. Instr. and Meth. **A490**, 132.
- [22] Aharrouche M *et al.* 2006, Nucl. Instr. and Meth. **A568**, 601.
- [23] Albrow M *et al.* 2002, Nucl. Instr. and Meth. **A487**, 381.
- [24] Bernardi E *et al.* 1987, Nucl. Instr. and Meth. **A262**, 229.
- [25] d'Agostini G *et al.* 1989, Nucl. Instr. and Meth. **A274**, 134.
- [26] Constantini F *et al.* 1998, Nucl. Instr. and Meth. **A409**, 570.
- [27] Acosta D *et al.* 1991, Nucl. Instr. and Meth. **A308**, 481.
- [28] Buskulic D *et al.* 1995, Nucl. Instr. and Meth. **A360**, 481.
- [29] *TESLA Technical Design Report* 2001, report DESY 2001-011, DESY, Hamburg, Germany.
- [30] Lobban O, Sriharan A and Wigmans R 2002, Nucl. Instr. and Meth. **A495**, 107.
- [31] CALICE Collaboration 2007, *Report to the Calorimeter R&D Review Panel*, ILC Report ILC-DET-2007-024.
- [32] Ferrando A *et al.* 1997, Nucl. Instr. and Meth. **A390**, 63.
- [33] Nagaslaev V, Sill A and Wigmans R 2000, Nucl. Instr. and Meth. **A462**, 411.
- [34] Akchurin N *et al.* 2004, Nucl. Instr. and Meth. **A533**, 305.
- [35] Akchurin N *et al.* 2005, Nucl. Instr. and Meth. **A536**, 29; **A537**, 537; **A548**, 336; **A550**, 185.